LABORATORI NAZIONALI DI FRASCATI

SIS – Pubblicazioni

LNF–94/035 (P)
24 Giugno 1994

The Dual Parton Model at Cosmic Ray Energies

J. Ranft
INFN – Laboratori Nazionali di Frascati, P.O. Box 13, I–00044 Frascati (Roma) Italy

Abstract

The Dual Parton Model for hadron–hadron, hadron–nucleus and nucleus–nucleus collisions is studied in the fragmentation region up to the Cosmic Ray energy region. Due to the excellent Feynman scaling behaviour of the model outside the regions around $x_F = 1.$ and $x_F = 0.$, it is found, that accelerator data in the fragmentation region are indeed relevant for the Cosmic Ray energy region. However, not enough data are available in the fragmentation region of hadron collisions with light target nuclei. Therefore many features of hadron production in collisions involving nuclei can only be extracted from the study of models.

PACS.: 13.85.Hd; 13.85.Ni; 13.85.Tp

(Submitted to Phys. Review D1)

I. INTRODUCTION

A hadron production model to be used at Cosmic Ray energies should take into account all possible information from fixed target experiments and collider experiments at accelerators. There are however important differences: For studying the Cosmic Ray cascade, the main interest is in the forward fragmentation region of hadron–nucleus and nucleus–nucleus collisions. Best studied at accelerators is the central region in hadron–hadron collisions.

In this paper we will discuss hadron production in the framework of the Dual Parton Model with emphasis in the fragmentation region. Important for Cosmic Ray studies are two aspects of multiparticle production:

(i)The change of particle production with energy, starting from the region well studied at present accelerator experiments.

(ii)The dependence of particle production on the nuclear target (and projectile).

A model for hadronic and nuclear interactions to be used in Cosmic Ray physics should provide the basic hadronic interaction term for the Cosmic Ray cascade. It should provide the cross sections for hadron–hadron, hadron–nucleus and nucleus–nucleus collisions as function of the energy. Secondary π^0 and η mesons are the source of the electromagnetic shower, secondary $\pi^{\pm}$ and $K^{\pm}$ mesons are the source of Cosmic Ray Muons and the source of atmospheric Neutrinos produced by the Cosmic Ray cascade. Secondary charmed mesons are the source for prompt Muons and Neutrinos. The model should work from the pion production threshold up to the highest possible primary energies.

Soft multiparticle production characterizing hadronic interactions at supercollider or Cosmic Ray energies cannot be understood purely within theoretical approaches provided by perturbative QCD. The nonperturbative soft component of hadron production, which is responsible for all of hadron production at low energies is still acting at higher energies.

The energy dependence of hadron production has so far been best studied in hadron–hadron collisions.

Using basic ideas of the dual topological unitarization scheme [1, 2] the Dual Parton Model (DPM) (a recent review is given in Ref.[3]) has been very successfully describing soft hadronic processes.

Observations like rapidity plateaus and average transverse momenta rising with energy, KNO scaling violation, transverse momentum–multiplicity correlations and *minijets* pointed out, that soft and hard processes are closely related. These properties were understood within the two–component Dual Parton Model [4–10].

The hard component is introduced applying lowest order of perturbative hard constituent scattering [11]. Single diffraction dissociation is represented by a triple–pomeron exchange (high mass single diffraction) and a low mass component.

The Dual Parton model provides a framework not only for the study of hadron–hadron interactions, but also for the description of particle production in hadron–nucleus and nucleus–nucleus collisions at high energies. Within this model the high energy projectile undergoes a multiple scattering as formulated in Glaubers approach; particle production is again realized by the fragmentation of colorless parton–parton chains constructed from the quark content of the interacting hadrons.

In Section II we give a short account of the Dual Parton Model. Section III describes the Monte Carlo event generator DPMJET–II used in this paper. We study with DPMJET–II hadron–hadron collisions in Section IV, hadron–nucleus collisions in Section V and nucleus–nucleus collisions in Section VI. The properties of the model relevant at Cosmic Ray energies are discussed in Section VII and a Summary is given in Section VIII.

II. THE DUAL PARTON MODEL

A. The energy dependence of multiparticle production and the two–component Dual Parton Model for hadron–hadron collisions

The soft input cross section in our unitarization scheme is described by the supercritical pomeron

$$\sigma_s = g^2 s^{\alpha(0)-1} \tag{1}$$

with g being the effective proton–pomeron coupling constant and $\alpha(0)$ the pomeron intercept. The corresponding pomeron–trajectory is given by $\alpha(t) = \alpha(0) + \alpha' t$. The supercritical pomeron was used in the two–component DPM from the beginning [4]. In all fits of the pomeron parameters to cross section data , we get consistently better fits with the supercritical pomeron than with the critical one.

Besides the supercritical soft (Fig.1(a)) and the hard pomeron (Fig.1(b)) we introduce graphs with pomeron–pomeron couplings. Provided that the pomeron–pomeron coupling constant Γ is small in comparison with other couplings, such as g, it is sufficient to consider the expansion in Γ only up to first order [5] . Thus a correction to the pure pomeron–exchange is represented by the triple–pomeron graph (Fig. 1(c)). included with an input cross section

$$\sigma_{TP} = \frac{2}{16\pi} \frac{g^3 \Gamma}{b_{sd}} ln \frac{s}{s_0} \tag{2}$$

where b_{TP} is the slope $b_{TP} = b^0_{TT} + 2\alpha' ln(s)$, $b^0_{TP} = 3.7\ GeV^{-2}$, $\alpha' = 0.24\ GeV^{-2}$ and $s_0 = 100\ GeV^2$. (The numbers given here are the ones used in the first published model [5], the results of our latest fits are given in [10].) The simplest cut of the triple–pomeron (Fig. 1(c)) corresponds to a high mass single diffractive interaction. High mass diffraction is a comparatively rare process. High mass means that the diffractively excited system should not be a well defined hadron resonance. We also describe high mass double diffractive processes again to first order introducing loop graphs (Fig. 1(d)), with a cross section

$$\sigma_L = \frac{1}{16\pi}\frac{g^2\Gamma^2}{2b_{DD}}(ln^2\frac{s}{s_0} + ln^2\frac{s_0'}{s} - 2ln^2\frac{5}{20}) \tag{3}$$

with b_{DD} being the slope parameter $b_{DD} = 2\alpha' ln(s)$, $s_0 = 400\ GeV^2$, and $s_0' = 25\ GeV^2$.

The input cross section for semihard multiparticle production σ_h is calculated applying the QCD improved parton model, the details are given in Ref.[4, 7, 8, 12].

$$\sigma_h = \sum_{i,j}\int_0^1 dx_1 \int_0^1 dx_2 \int d\hat{t}\ \frac{1}{1+\delta_{ij}}\frac{d\sigma_{QCD,ij}}{d\hat{t}}\ f_i(x_1,Q^2)f_j(x_2,Q^2)\ \Theta(p_\perp - p_{\perp thr}) \tag{4}$$

$f_i(x,Q^2)$ are the structure functions of partons with the flavor i and scale Q^2 and the sum i,j runs over all possible flavors. To remain in the region where perturbation theory is valid, we use a low $p_\perp$ cut–off $p_{\perp_{thr}}$ for the minijet component. Furthermore, since we calculate $\sigma_{QCD,ij}$ in lowest-order QCD perturbation theory we multiply the hard input cross section σ_h with a K factor in the range of 1.5 to 2. A hard interaction leads to a chain system shown in Fig. 1(b).

The momentum fractions of the constituents at the ends of the different chains are sampled using the exclusive parton distribution, which has the form for an event with n_s soft and $n_h(n_h \geq 1)$ hard pomerons

$$\rho(x_1,...,x_{2n_s},...,x_{2n_s+2+n_h}) \sim \frac{1}{\sqrt{x_1}}(\prod_{i=3}^{2n_s+2}\frac{1}{\sqrt{x_i}})x_2^{1.5}\prod_{i=2n_s+3}^{2n_s+2+n_h} g(x_i,Q_i)\delta(1-\sum_{i=1}^{2n_s+2+n_h} x_i). \tag{5}$$

The distributions $g(x_i,Q_i)$ are the distribution functions of the partons engaged in the hard scattering. The Regge behaviour of the soft valence quark x–distributions is $x^{-0.5}$, the term $1/\sqrt{x_1}$ refers to the valence quark at the end of a soft valence chain. The Regge behaviour of a diquark x–distribution is $x^{1.5}$, the term $x_2^{1.5}$ refers to the x–distribution of the valence diquark at the end of a soft valence chain. The Regge behaviour of soft sea–quark x–distributions agrees to the one of the valence quarks,

it is also $x^{-0.5}$. The terms $1/\sqrt{x_i}$ refer to the sea–quarks and sea–antiquarks at the end of soft sea chains.

Here one remark is in order. In the previous papers [5], [10] we did use terms $1/x_i$ for the soft sea–quarks and antiquarks. A corresponding formula with $1/x_i$ is also given in the Dual Parton Model review [3]. The use of this different behaviour for the soft sea–quark x–distributions was certainly motivated by the behaviour of the deep inelastic x–distributions for sea–quarks, but it is not correct for the soft sea quarks. The correct Regge behaviour of soft sea quarks was already discussed in an Appendix to the paper of Capella and Tran Thanh Van [13] and it is also given for instance in [14]. It is easy to check, that at low energies, typical for fixed target experiments, the correct form $1/x$ or $1/\sqrt{x}$ is not very important, the behaviour is mainly determined by the low x cut–off of the structure functions.But for our goal, to study the Feynman x_F–distributions of hadrons at the highest energies in the fragmentation region, it is essential to use the correct form $1/\sqrt{x}$.

Soft(s), hard(h), high mass single diffractive(TP), and high mass double diffractive(L) processes are treated simultaneously within an eikonal unitarization scheme using the impact parameter representation

$$\chi_i(B,s) = \frac{\sigma_i(s)}{8\pi b_i}\exp[-\frac{B^2}{4b_i}], \qquad i = s,h,TP,L \tag{6}$$

normalized by

$$\int 2\chi_i(B,s)\,d^2B = \sigma_i \tag{7}$$

with b_h energy independent, $b_s = b_{TP} = b_L = b + \alpha' log(s)$. The exclusive cross section for l_c cut soft pomerons, m_c cut hard pomerons, n_c cut triple–pomeron graphs and p_c cut loop graphs is given by

$$\sigma(l_c,m_c,n_c,p_c,B,s) = \frac{(2\chi_s)^{l_c}}{l_c!}\frac{(2\chi_h)^{m_c}}{m_c!}\frac{(-2\chi_{TP})^{n_c}}{n_c!}\frac{(-2\chi_L)^{p_c}}{p_c!}\exp[-2\chi(B,s)] \tag{8}$$

with

$$\chi(B,s) = \chi_s(B,s) + \chi_h(B,s) - \chi_{TP}(B,s) - \chi_L(B,s). \qquad (9)$$

The total and elastic cross section are given by

$$\sigma_{tot} = 4\pi \int_0^\infty BdB(1 - \exp[\chi(B,s)]), \quad \sigma_{el}(B,s) = \frac{1}{4}[\sigma_{tot}(B,s)]^2. \qquad (10)$$

Diffractive processes characterized by the excitation of an initial hadron to intermediate resonances (low mass diffractive interactions) are introduced via a two channel eikonal formalism. As suggested in Ref.[5] a new coupling λ modifies the three graphs given in Fig. 1(e-g) and leads to a modification of each graph with l soft, m hard, n triple–pomeron, and p loop exchanges.

During 1992–3 new data on deep inelastic scattering and new fits to parton structure functions were reported. New features of these fits include (i) the flavor dependence of sea–quark distributions and (ii) a stronger rise of the structure functions at low x–values, that is in the region important for minijets. These fits by Martin Roberts and Stirling [15] and by the CTEQ–Collaboration [16] include functions with a conventional $1/x$ singularity of sea–quark and gluon distributions (for instance the MRS[D0] functions) as well as functions with a $1/x^{1.5}$ singularity (for instance the MRS[D–] functions). The pre–HERA measurements did not allow to decide between these two possibilities. However, there were theoretical arguments in favor of the $1/x^{1.5}$ singularity [17]. These more singular parton distributions were in the past used to calculate the minijets [7,8], but not taken very seriously. This was changed in [10] , since the first HERA–data seem to favor just these singular parton distribution functions [18].

Gluons are the most important source of minijets, unfortunately, so far no HERA data for the gluon distributions are available, but we should start now to discuss the implementation of the more singular functions for minijets.

In order to remove an inconsistency in older versions of DTUJET with $x^{-1.5}$ singular structure functions we make in DTUJET-93 [10] the threshold for minijet

production $p_{\perp thr}$ energy dependent in such a way, that at no energy and for no PDF the resulting σ_h is bigger than the total cross section. Then at least we have a cross section, which is indeed mainly the cross section of a $2 \to 2$ parton process at this level, but we can get back to the real $2 \to n$ processes via parton showering. One possible form for this energy dependent cut off is:

$$p_{\perp thr} = 2.5 + 0.12[\lg_{10}(\sqrt{s}/\sqrt{s_0})]^3 \quad [GeV/c], \quad \sqrt{s_0} = 50GeV. \tag{11}$$

The resulting σ_h are smaller than the total cross sections resulting after the unitarization for all MRS-92 and CTEQ PDF's and also the older KMRS [19] distributions.

DTUJET93 [10] has been compared with nearly all aspects of hadron production in the central region as found at the CERN and Fermilab colliders. Extrapolating to LHC energies, we get charged plateaus of 5–6 particles per pseudorapidity unit for the models with all MRS-92 and CTEQ PDF's. However, the average transverse momenta in the models with the singular PDF's rise more steeply with energy than in previously published versions of DTUJET. We find using DTUJET93 at LHC energies an average $p_\perp$ typically 100 MeV/c bigger than previously.

The two–component Dual Parton Model has some natural way to cut–off the singularity of the minijet cross section at low $p_\perp$. The model uses the soft pomeron cross section as the low $p_\perp$ limit of the minijets.

B. The Dual Parton Model for hadron production in hadron–nucleus and nucleus–nucleus collisions

The first successfull applications of the Monte Carlo version of the dual parton model (DPM) to hadron–nucleus [20, 21] and nucleus–nucleus [22–24] collisions also demonstrated that the cascade of created secondaries in the target (and projectile) nuclei contributes significantly to particle production in the target (and projectile) fragmentation regions. On the other hand, it is known for many years that a naive treatment of intranuclear cascade processes on the basis of elementary cross sections

overestimates the particle yields, if the incident energy significantly exceeds five or ten GeV [25, 26].

This problem may be solved by introducing the concept of a formation zone [27, 28] suppressing in a natural way the cascading of high–energy secondaries. The Monte Carlo model includes intranuclear cascade processes of the created secondaries combined with the formation time concept since the version DTUNUC–1.00.

In the following we briefly sketch the basic ideas of the model and mention the most important ingredients; for a more detailed description of the model as applied in the code we refer to Refs. [20, 21, 29–33].

1. The Monte Carlo realization of the dual parton model DTUNUC for hadron-nucleus and nucleus-nucleus collisions

The model starts from the impulse approximation for the interacting nuclei – i.e. with a frozen discrete spatial distribution of nucleons sampled from standard density distributions [34]. The primary interaction of the incident high–energy projectile proceeds via totally n elementary collisions between $n_p = n_A$ and $n_t = n_B$ nucleons from the projectile (for incident hadrons $n_p = 1$) and the target nuclei, resp. Actual numbers n, n_p and n_t are sampled on the basis of Glauber's multiple scattering formalism using the Monte Carlo algorithm of Ref.[34]. Note that individual hadrons may undergo several interactions. Particle production in each elementary collision is descibed in DTUNUC by the fragmentation of two color–neutral parton–parton chains. In DPMJET also multiple soft chains and multiple minijets are considered. Those chains are constructed from the valence quark systems or – in the case of repeated scatterings of single hadrons – from sea–$q\bar{q}$ pairs and sea–$qq - \bar{q}\bar{q}$ pairs of the interacting hadrons.

For nucleus–nucleus collisions in the two–chain approximation the single particle densities are given by

$$\frac{dN^{AB}}{dy} = \frac{1}{\sigma_{AB}} \sum \sigma_{n_A,n_B,n} \{ \Theta(n_B - n_A)[n_A(N^{qq^A - q_v^B} + N^{q_v^A - qq^B})$$
$$+(n_B - n_A)((1-\alpha)(N^{q_s^A - qq^B} + N^{\bar{q}_s^A - q_v^B}) + \alpha(N^{(\bar{q}\bar{q})_s^A - qq^B} + N^{(qq)_s^A - q_v^B}))$$
$$+(n - n_B)((1-2\alpha)(N^{q_s^A - \bar{q}_s^B} + N^{\bar{q}_s^A - q_s^B})$$
$$+\alpha(N^{q_s^A - (qq)_s^B} + N^{(qq)_s^A - q_s^B}) + \alpha(N^{\bar{q}_s^A - (\bar{q}\bar{q})_s^B} + N^{(\bar{q}\bar{q})_s^A - \bar{q}_s^B}))]$$
$$+(A \to B)\} \qquad (12)$$

Here n denotes the total number of inelastic collisions between n_A and n_B participating nucleons from the projectile and target nuclei and α is the rate of diquark pairs to $q - \bar{q}$ pairs in the proton sea .

The hadronization of single chains is handled by the Monte Carlo codes BAMJET [35, 36] and DECAY [37] or by the Lund code JETSET–7.3 [38].

2. The Cronin effect

In nuclear collisions, the partons at the sea and valence chain ends carry transverse momenta from different sources: (i)The intrinsic parton transverse momentum in the hadron. (ii) A transverse (and longitudinal) momentum resulting from the Fermi motion of the nucleons inside the nucleon. These first two kinds of transverse momentum were implemented into DTUNUC from the beginning. (iii) During the passage of the chain end partons through nuclear matter, they suffer nuclear multiple scattering which changes (usually increases) their transverse momenta.

The multiple scattering of partons is known since a long time to be responsible for the so called *Cronin effect* [39] of particle production at large transverse momentum on nuclear targets. A similar enhancement of particle production in hadron–nucleus and nucleus-nucleus collisions compared to hadron–hadron collisions has been observed in many experiments already at rather modest $p_\perp$. (See for instance the review of experimental data of Schmidt and Schukraft [40] where the data of these $p_\perp$ ratios

are collected in Figs.4.21 to 4.24.)

At large $p_\perp$ this effect can be studied calculating the parton scattering pertubatively. Our rather low $p_\perp$ sea chain ends might be considered as the low $p_\perp$ limit of perturbatively scattered partons. We apply to them and to the hard scattered partons multiple scattering taking into account their path length inside the nuclear matter and adjust the parameters in such a way, that the measured $p_\perp$ ratios at rising transverse momenta are approximately reproduced by the code DTUNUC.

3. Production of strange particles

Studies of strangeness production within this model were given in [32, 33]. The DPM is an independent string model. Since the individual strings are universal building blocks of the model, the ratio of *produced* strange particles over non–strange ones will be approximately the same in all reactions. However, since some strings contain sea quarks at one or both ends and since strange quarks are present in the proton sea, it is clear, that, by increasing the number of those strings, the ratio of strange over non–strange particles will increase. This will be the case for instance, when increasing the centrality in a nucleus–nucleus collision. It is obvious, that the numerical importance of the effect will depend on the assumed fraction of strange over non–strange quarks in the proton sea. The rather extreme case leading to a maximum increase of strangeness is to assume a SU(3) symmetric sea (equal numbers of u, d and s flavors). We express the amount of SU(3) symmetry of the sea chain ends by our parameter s^{sea} defined as $s^{sea} = 2 < s_s > /(< u_s > + < d_s >)$ where the $< q_s >$ give the average numbers of sea quarks at the sea chain ends. All results from DPMJET–II given in this paper are obtained with s^{sea}=0.5 . However, the above scenario has an important draw–back. Since an antiquark from the sea is always attached to a valence– or sea–quark on the opposite hemisphere, and since the only important strings at CERN–energies are those containing at least a diquark at one end, it will be impossible to obtain an enhancement of antibaryons. In fact, due to

energy–momentum conservation, the ratio $\bar{\Lambda}/h^-$ will in fact decrease with increasing centrality. In an attempt to solve this problem, we allow the creation of $qq - \bar{q}\bar{q}$ pairs from the proton sea, leading to the production of strings of type $\bar{q}\bar{q} - \bar{q}$ or $\bar{q}\bar{q} - qq$ in which the production of strange antibaryons will be easier. The rate α of diquark pairs to $q - \bar{q}$ pairs in the proton sea is assumed to be the same as the ratio of $q \to (qq)$ to $q \to q$ branching in the chain fragmentation.

4. Diffractive events

Single diffraction within the Dual Parton Model was studied in detail and compared to experimental data in [9, 41]. Single diffraction dissociation is represented by a triple–Pomeron exchange (high mass single diffraction) and a low mass component (low mass single diffraction) [5].

Diffractive processes characterized by the excitation of an initial hadron to intermediate resonances (low mass diffractive interactions) are introduced via a two channel eikonal formalism.

III. THE EVENT GENERATOR DPMJET-II

The event generator DPMJET-I for hadron–hadron, hadron–nucleus and nucleus–nucleus collisions described in [42] was based on DTUNUC-1.0 [43] and DTUJET90 [5] DPMJET-I uses the Dual Parton Model for nuclear collisions as implemented in DTUNUC-1.0, but for each elementary nucleon–nucleon collision the full system of multiple soft chains and multiple minijets as implemented in DTUJET90 is used. DPMJET-I was mainly used in the past to study nucleus–nucleus collisions at the energies of the CERN-SPS and the future heavy ion colliders RHIC and CERN-LHC [42].

DPMJET, version II is a code similar to DPMJET-I, but it has been constructed completely new on the basis of the much improved codes DTUNUC-1.04 [33] and DTUJET93 [10]. Here we report on the study, using DPMJET-II of hadron–hadron, hadron–nucleus and nucleus–nucleus collisions in the Cosmic Ray energy region. No similar studies were undertaken with the previous version of DPMJET. So far no central nucleus–nucleus collisions at RHIC or the CERN-LHC were simulated with DPMJET-II, this will be done in due course. We expect with DPMJET-II mainly a rise of the average transverse momenta in nucleus–nucleus collisions against DPMJET-I. The reason for this is the increase of average transverse momenta at cms energies in the TeV region in DTUJET93 against DTUJET90 and the implementation of the Cronin effect in DTUNUC-1.04 (and with this in DPMJET-II). This leads to a further rise of average transverse momenta in hadron–nucleus and nucleus–nucleus collisions against hadron–hadron collisions.

IV. HADRON–HADRON COLLISIONS WITH DPMJET–II

A. Proton–proton collisions

1. Average multiplicities of produced hadrons in p–p collisions

DPMJET–II, using he multiple soft chains and multiple minijets from DTUJET93, is expected to show the same rise like DTUJET93 with energy of average multiplicities, the rapidity plateau and of average transverse momenta.

In Table 1 we compare DPMJET–II at 200 GeV with multiplicities of the most important secondary hadrons. The data are from Ref. [44]. The agreement is excellent.

2. Feynman scaling

The relevance of an event generator like DPMJET–II based on the Dual Parton Model for hadron production cross sections in the Cosmic Ray energy region can only be claimed, if the model (i) agrees to the best available data in the accelerator energy range and (ii)shows a smooth behaviour in the extrapolation to higher energies.

For the Cosmic Ray cascade in .the atmosphere only hadron–nucleus collisions are relevant, with Nitrogen N beeing the most important target nucleus. However, experimental data in the projectile fragmentation region are of much better quality in hadron–hadron , and especially proton–proton collisions than for collisions of hadrons with light nuclei. Therefore, we start with the study of proton–proton collisions.

In order to see, whether data in the accelerator energy range with projectile energies well below 1 TeV are relevant at all, we study first the Feynman scaling behaviour of the model. In Figs. 2 and 3 we study the Feynman scaling of the produced leading baryons and the secondary π^+ mesons. In most of the x_F region , say for $0.05 \leq x_F \leq 0.8$, we find Feynman scaling indeed very well satisfied in the Dual Parton Model. The violations of Feynman scaling, which occur around $x_F = 0$ are connected with the well known rise of the rapidity plateau for all kinds of produced particles. This

violation is only absent for the leading baryon, where the x_F distribution vanishes at $x_F = 0$. We find also a strong violation of Feynman scaling for secondary nucleons around $x_F = 1$. This is connected with the diffractive component, which clearly violates Feynman scaling. For produced mesons, the statistics is not good enough, to conclude, whether Feynman scaling near $x_F = 1$ is strongly violated, but the diffractive component should also lead to a violation for the meson distributions. However in the Feynman x_F region most important for the Cosmic Ray cascade $0.1 \leq x_F \leq 0.6$, Feynman scaling also for the meson distributions is excellent. This means, within the framework of the Dual Parton Model, experimental data in the fragmentation region (and the agreement of the model to them) are indeed very relevant also for the Cosmic Ray energy region.

3. Comparing to experimental Feynman x_F distributions

In proton–proton collisions, we have the advantage that experimental data are available for Feynman x_F distributions $d\sigma/dx_F$ or $x_F d\sigma/dx_F$ integrated over transverse momentum. In hadron–nucleus collisions nearly all data are only double differential distributions. In the Monte Carlo calculation, we get much smaller error bars for single differential distributions than for double differential distributions. However, also in proton–proton collisions, the data at times contradict each other.

Let us start to discuss π^+ and π^- production. The EHS–NA22 Collaboration [45] has data on $d\sigma/dx_F$ in 250 GeV proton–proton collisions. In Fig. 4 we compare the DPMJET results for π^- production in the forward and backward fragmentation regions and find a reasonable agreement. In Fig. 5 we compare with the production of positively charged hadrons for $x_F \geq$ -0.4 and with π^+ production for $x_F \leq$ -0.4, again the agreement is reasonable. In the projetile fragmentation region at large x_F this distribution is dominated by the leading protons from diffractive and nondiffractive events.

Comparing to π^+ ad π^- production from other experiments, we get problems. In

Fig. 6 we compare with data from Aguilar–Benitez et al. [46] and Bailly et al. [47] for $x_{F,lab} d\sigma/dx_{F,lab}$ at 400 and 360 GeV. Because of the excellent Feynman scaling found above, we have these two comparisons in one plot. In the case of π^- production in Fig. 6 both sets of data agree very well and also the model agrees very well to the data. in the region $x_{F,lab} \leq 0.5$, where the error bars are small. Contrary, in the case of π^+ production (not shown) both sets of data disagree strongly (this was already noted by Aguilar–Benitez et al.[46]) Furthermore, the data of Aguilar–Benitez et al. shows a strange structure at $0.5 \leq x_{F,lab} \leq 0.8$, which is not found in other experiments and in the model. Finally, we note, that the model is well below the data of Bailly et al. [47], It seems, that there is an error in the normalization of these data, therefore, we ignore the comparison with these data.

We turn to the comparison with the data of Kafka et al. [48] and Brenner et al. [49] at 205 and 175 GeV. Because of the excellent Feynman scaling found above, we again compare to both experiments in one plot, Fig. 7 for π^+ . This time we find for π^+ a very good agreement of both experiments, but the two sets of π^- data (not shown) are not fully consistent . In the low $x_{F,lab}$ region with good statistics, we find the model for π^+ production is slightly below the data, in addition, at large $x_{F,lab}$, in the regin dominated by diffractive production, there is evidence, that the model overestimates the π^+ s well as π^- production, this region is however not the dominant region, from where Cosmic Ray Muons result.

4. Transverse momentum dependence of DPMJET–II in proton–proton collisions and the seagull effect

In Fig. 8 we repeat one of the comparisons already performed with DTUJET93 [10], this time with DPMJET–II and find the same agreement with the collider data on the $p_\perp$ distribution at $\sqrt{s} = 200$ GeV. The comparison in Fig. 8 is for the central region with pseudo rapidities $|\eta| \leq 2.5$. This is not very relevant for the fragmentation region. In the fragmentation region the transverse momentum distributions and aver-

age transverse momenta are known to depend strongly on Feynman x_F. This effect is known under the name *seagull effect*. In Figs. 9 and 10 we compare DPMJET–II with data on the seagull effect measured by the EHS–RCBC Collaboration at 360 GeV and find a reasonable agreement. Unfortunately, experimental data on the seagull effect are usually limited to $x_F \leq 0.5$–0.6.

5. Strange particle production in the fragmentation region of proton–proton collisions

Charged K–mesons are besides the charged Pions the most important source of Cosmic Ray Muons and Neutrinos. Therefore, we have to check, how well the strange hadron production is described by DPMJET–II. In Fig. 11 we compare the K^+ distribution $x_F d\sigma/dx_F$ with data from Aguilar–Benitez et al. [46] at 400 GeV. The agreement is reasonable, but the model does not reproduce the structure seen in the data.

In Fig. 12 we compare $x_F d\sigma/dx_F$ for Λ Hyperons with the experiments of Kichimi et al. [50] at 400 GeV and of Bailly et al. [51] at 360 GeV. The agreement of both experiments with each other and the agreement of model and data are excellent, but the experimental errors and the statistical errors of the Monte Carlo calculation are quite big . In Fig. 13 we compare with the K^0_S distributions from the same two experiments. At small values of x_F, where the statistics of data and Monte Carlo calculation is still good enough, we find good agreement.

In Fig. 14 we compare with the data for the seagull effect for Λ production, the agreement is reasonable. The model reproduces for Λ production the remarkable feature of the data, that the average transverse momentum is nearly independent on x_F.

Finally in Fig. 15 we compare the K^+/π^+ ratios as function of the transverse momentum with data of Antreasyan et al. [52]. The model reproduces well the rise of these ratios with transverse momentum.

A stringent test of the model and particularly of the assumption of an enhanced

strange sea is provided by the behaviour of the average strange particle multiplicities (or better of the ratio of strange over non–strange ones) as a function of either the collision energy $\sqrt{s}$ or the charged particle density. The $\sqrt{s}$–dependence is presented in Fig.16 and the dependence on the charged plateau of the ratio K/π is presented in Fig.17. We compare to data of the Fermilab–E735 Collabration [53, 54]. For these calculations at high energies in p + p collisions we use the two–component Dual Parton Model in the form of DTUJET93 [10].

B. Pion–proton and Kaon–proton collisions

In the Cosmic Ray cascade beyond the first generation the interactions of secondary hadrons, mainly Pions and Kaons are as important or even more important than the interaction of nucleons. The Dual Parton Model can be constructed for all hadronic projectiles. It is only required, to know the flavors of the valence quarks in order to predict the hadron production by hadronic projectiles.

In this Section we compare the hadron production in Pion–proton and Kaon–proton collisions as implemented in DPMJET–II with data in the fragmentation region.

In Figs. 18 and 19 we compare the model with the results of the EHS–NA22 experiment [45] at 250 GeV in π^+–p collisions. As in the corresponding comparisons with this experiment for p–p collisions, we find a satisfactory agreement of model and data. This refers to the produced π^- as well as to the leading π^+ mesons and to the diffractive peak in the leading particle distribution.

In Fig. 20 we compare at 175 GeV to data on $\pi^+ + p \rightarrow \pi^+ + X$ and $\pi^+ + p \rightarrow \pi^- + X$ from Brenner et al. [49]. In Fig. 21 we compare at 175 GeV to data on $K^+ + p \rightarrow K^+ + X$, $K^+ + p \rightarrow \pi^+ + X$ and $K^+ + p \rightarrow \pi^- + X$ from Brenner et al. [49]. In all of these comparisons we find a quite good agreement between the model and the data. We conclude, that the Dual Parton Model is able to describe hadron production in meson–nucleon collisions as well as in nucleon–nucleon collisions.

V. HADRON–NUCLEUS COLLISIONS WITH DPMJET–II

A. Hadron–Air inelastic cross sections as function of the energy

The Glauber model, which is part of DPMJET–II allows to calculate the inelastic hadron–nucleus cross sections. What we need for this calculation is the nuclear geometry and the elementary hadron–nucleus scattering amplitude parametrized as follows:

Energy dependent quantities enter the Glauber approach via the profile function of elastic hadron-nucleon scattering,

$$\gamma_{hN}(b) = \frac{1}{2\pi ip} \int d^2q \exp(i\vec{q}\cdot\vec{b}) f_{hN}(\vec{q}), \tag{13}$$

i.e. the amplitude of elastic hadron-nucleon scattering in the impact parameter representation (with $\vec{q}$ denoting the lateral, i.e. two-dimensional momentum transfer). In their Monte Carlo realization of Glauber's approach Shmakov et al. [34] apply the high-energy approximation of the profile function,

$$\gamma_{hN}(b) = \frac{\sigma_{hN}^{tot}}{4\pi a}\left(1 - i\frac{\Re f_{hN}(0)}{\Im f_{hN}(0)}\right) e^{-\frac{b^2}{2a}}, \tag{14}$$

with parameters σ^{tot}, a and $\rho = \Re f_{hN}(0) \;/\; \Im f_{hN}(0)$ appropriate for the description of nucleus-nucleus interactions at energies of several GeV per nucleon. (This parametrization corresponds to a differential cross section $d\sigma/dt \simeq \sigma_{tot} \exp(a \cdot t)$ with $t \simeq -\vec{q}^2$.)

However, the energy dependence of the elastic hadron-nucleon scattering amplitudes will influence the properties of hadron–nucleus and nucleus–nucleus scattering. In particular, the number of individual high-energy hadron-nucleon interactions (n, n_A, n_B) will increase with rising energy, hence the multiplicity will increase stronger than to be expected from the energy dependence of single hadron-hadron interactions.

Guided by the data collected in Ref. [55], we apply the following parametrizations for the slope parameter a : $a = 8.5\ (1 + 0.065 \ln s)$ for nucleon-nucleon collisions and

$a = 6.0\ (1 + 0.065 \ln s)$ for $\pi-$ and K–nucleon collisions. We use for the ratio ρ of the real and imaginary part of the elastic scattering amplitude: $\rho = -0.63 + 0.175 \ln \sqrt{s}$ for the energy region $3.0 \leq \sqrt{s} \leq 50.$ and $\rho = 0.1$ in the energy region $\sqrt{s} \geq 50$ GeV in nucleon-nucleon scattering and $\rho = 0.01$ for $\pi-$ and K–nucleon scattering.

The energy dependence of the total cross sections is described by the fits of the Particle Data Group [56]; at energies beyond the range of the actual parametrization of the pp cross section the one for $\bar{p}p$ is applied and at energies even higher we use the total cross–sections as calculated by the two–component Dual Parton Model for hadron–hadron collisions [10].

The same information is also needed to construct the inelastic events and indeed usually each run of DPMJET starts with a calculation of the inelastic cross section.

In Fig. 22 we compare the p–Air cross sections calculated with DPMJET–II to data from Cosmic Ray experiments.

B. Feynman scaling in hadron–nucleus collisions

In order to understand the relevance of accelerator data on particle production in hadron–nucleus collisions for the Cosmic Ray cascade, we study again the Feynman scaling behaviour of p+Air$\rightarrow \pi^+ +$X. This is done in Fig. 23 , where we plot the $x_F dN/dx_F$ distributions for laboratory energies of 1, 10, 100 and 1000 TeV. As above in proton–proton collisions, we find again , that Feynman scaling is very well satisfied in most of the x_F region. Exceptions are again the region around $x_F = 0$, where the rise of the rapidity plateau violates Feynman scaling and the region x_F =1 for leading particles, where the diffractive component does not show Feynman scaling. Given this Feynman scaling behaviour, we can again conclude, that accelerator data and their agreement to the model are indeed very relevant to the Cosmic Ray application of the model.

C. Feynman x distributions in collisions of protons with light nuclei and the $\alpha(x_F)$ behaviour

In Fig.24 we compare at 400 GeV the Feynman x_F distributions of produced protons and π^+ mesons in proton–proton, proton–Beryllium, proton–Air, proton–Aluminium and proton–Copper collisions as calculated with DPMJET–II. We observe in the relevant x_F region the x_F distributions from p–p to p–Air to differ by less than a factor 2 and the distributions changing the target from p–Be over p–Air to p–Al again to change by less than a factor 2. The latter change can be described by $\alpha(x_F)$ representing the cross section as

$$x_F \frac{d\sigma}{dx_F}^{p-A} = A^{\alpha(x_F)} x_F \frac{d\sigma}{dx_F}^{p-N} \tag{15}$$

For the transition p–p to p–Air this $A^{\alpha(x_F)}$ behaviour is not relevant, since we know that this kind of extrapolating h-A total cross sections to p–p does not give the correct p–p total cross section. Usually $\alpha(x_F)$ is determined using data for two or more different target nuclei without ever considering p–N collisions.

The x_F distributions for p–p and p–Air collisions in Figs. 24 cross in the region below $x_F = 0.2$. This crossing diminishes further the errors, which can result from errors in the p–p to p–Air transition. Unfortunately, there are no precise data (from the same experiment), where the differences of Feynman x_F distributions in p–p and p–light nucleus collisions could be checked. Therefore, for this transition, the best we can do at present is to rely on the model.

We do not learn much more, if we compare to experiments , where the hadron production on light target materials is measured in the form of double differential distributions. Such comparisons were done. The errors in such double differential comparison are usually rather big and difficult to understand.

The results of double differential cross sections for inclusive hadron production in hadron–nucleus collisions have been represented in the form

$$E\frac{d^3\sigma}{d^3p}^{p-A} = A^{\alpha(x_F,p_\perp)} E\frac{d^3\sigma}{d^3p}^{p-N} \tag{16}$$

With data on two different target nuclei, one can extract $\alpha(x_F, p_\perp)$ without the knowledge of $Ed^3\sigma/d^3p^{p-N}$. The data of Barton et al. [57] at 100 GeV and at a transverse momentum $p_\perp$ =0.3 GeV/c were used to get $\alpha(x_F)$ (in reality : $\alpha(x_F, p_\perp = 0.3GeV/c)$). In the Monte Carlo calculation it is difficult to get such a good statistics at fixed $p_\perp$, to extract meaningfull $\alpha(x_F)$ values. This is just possible for single differential distributions in x_F. In Fig. 25 we compare the $\alpha(x_F)$ as obtained by Barton et al. [57] for pion production at $p_\perp$ = 0.3 GeV/c with $\alpha(x_F)$ obtained from DPMJET–II results for all charged hadrons integrated over all $p_\perp$. The agreement in the x_F region of overlap is reasonable. For $x_F \to 0$ in the Dual Parton Model the limiting $\alpha(x_F)$ value is 1. This is actually also obtained from DPMJET–II. For large values of x_F the limiting $\alpha(x_F \to 1)$ for the data as well as for the Monte Carlo seems to be around 0.4.

The agreement with these $\alpha(x_F)$ data is the strongest point for the claim, that the Dual Parton Model in the form of the DPMJET–II event generator gives a good description of the nuclear dependence of hadron production in the fragmentation region. We stress however once again, these $\alpha(x_F)$ data are only for fixed $p_\perp$ and it would be highly desirably to obtain better data for the change of hadron production from proton–proton collisions to collisions of protons with light target nuclei.

D. Transverse momentum distributions in hadron–nucleus collisions , transverse momentum ratios and the $\alpha(p_\perp)$ behaviour

In Figs. 26 and 27 we compare transverse momentum distributions calculated with DPMJET–II for p–W and p–Au collisions at 200 GeV with data [58] and [59] and find a good agreement.

In order to show the changes in the transverse momentum distributions from p–p to p–A collisions one presents the data in the form of $p_\perp$ ratios

$$R(p_\perp) = \frac{E\frac{d^3N^{p-A}}{d^3p}}{E\frac{d^3N^{p-p}}{d^3p}} \tag{17}$$

or one uses the $\alpha(p_\perp)$ representation

$$E\frac{d^3\sigma^{p-A}}{d^3p} = A^{\alpha(p_\perp)}E\frac{d^3\sigma^{p-N}}{d^3p} \quad . \tag{18}$$

In Fig. 28 we compare DPMJET–II with $\alpha(p_\perp)$ data from Garbutt et al. [60]. The data are for identified kinds of secondary hadrons. In the model calculation we present $\alpha(p_\perp)$ only for π^+ and K^+. We find a rather good agreement with the data for π^+ , The $\alpha(p_\perp)$ calculated for K^+ are systematic above the values for π^+, but they stay in the region with good statistics below the data for the K^+.

In Fig. 29 we present the seagull effect as calculatd in DPMJET–II for p–Air collisions at energies between 1 TeV and 1000 TeV . At all energies $p_\perp(x_F)$ rises significantly with x_F (at least in the region $x_F \leq 0.5$.). At the same time the transverse momentum rises strongly with the collision energy, in the model mainly due to the rise of minijet production.

E. Production of strange particles in hadron–nucleus collisions

Important questions for Cosmic Ray studies are:

(i) Is there an enhancement of strange particle production if we go at the same energy from proton–proton to proton–nucleus collisions? and

(ii) Does in hadron–nucleus collisions the strange hadron production rise faster than the inelastic cross–section, or does the multiplicity ratio $n_{strange}/n_{nonstrange}$ increase with the mass A of the target nucleus?

One can look at multiplicities of strange and nonstrange hadrons from some experiments, (such data were collected by Bialkowska et al. [61]) . A look at such a compilation shows, that the statistical and systematical uncertainties of the data do not allow to draw any conclusion about a systematic increase or decrease.

Fortunately, there are some experiments, where the strange and nonstrange hadron production on different target nuclei is compared in the form A^{α} and α values are given separately for strange and nonstrange produced hadrons. We review the results of three of these experiments:

(i)Antreasyan et al.[52] measure the *Cronin effect* . They present (in their Fig.16) $\alpha_K - \alpha_\pi$ as function of $p_\perp$ and find it at all measured $p_\perp$ values to be larger than zero. This means, that the K/π ratio increases with A. Unfortunately, their lowest $p_\perp$ value is 0.77 GeV/c (where $\alpha_K - \alpha_\pi$ is around 0.07) and one might doubt, whether this allows a conclusion about all of the low-$p_\perp$ particle production.

(ii) An experiment similar to the one of Antreasyan et al.[52] was performed by Garbutt et al. [60], (see also Fig. 28) fortunately at $p_\perp$ values between 0.2 and 2.4 GeV/c. Also here , at all $p_\perp$ they find $\alpha_K - \alpha_\pi \approx 0.1$. In DPMJET–II we find $\alpha_{K^+} - \alpha_{\pi^+}$ systematically larger than zero, but smaller than 0.1. Again from the data as well as from the model, the conclusion is, that K/π increases systematically with A.

(iii)Skubic et al. [62] present α values as function of Feynman x_F and $p_\perp$ for K^0_S production at 300 GeV. α values are given for $x_F = 0.2$, 0.4 and 0.6 and $p_\perp$ values between 0 and 1.5 GeV/c. At $p_\perp$ values below 0.8 GeV/c all $\alpha(x_F, p_\perp)$ are found smaller than 2/3, but $\alpha(x_F, p_\perp)$ increases with decreasing x_F and we might hope, that in the x_F region around 0, from where the dominant $K^\pm$ and K^0 production comes, again $\alpha(x_F, p_\perp)$ is found bigger then 2/3. A modest rise of the K/π ratios with the mass of the target nucleus is also found in DPMJET–II, it is however difficult to get enough statistics to extract meaningfull α values from the Monte Carlo calculation.

VI. NUCLEUS–NUCLEUS COLLISIONS

A. Nucleus–Air inelastic cross sections as function of the energy

The same Glauber model, which gives the hadron–Air inelastic cross sections is also able to calculate nucleus–nucleus inelastic cross sections. In Fig. 30 we present nucleus–Air inelastic cross sections calculated with DPMJET–II in the energy range 0.1 TeV to 10^7 TeV. All these cross sections rise with the energy, but the relative rise of the cross sections from the lowest to the highest energy is smaller for heavy projectiles, since in the center, at small impact parameters the nuclei become black already at lower energies.

B. Comparison of nucleus–nucleus collisions according to DPMJET–II with the superposition model

Instead of the proper sampling of nucleus–nucleus scattering events, an approximation often applied is the so called superposition model. There are two different possible superposition models:

(i) A Nucleus–nucleus collision A–B with N_p participating projectile nucleons is approximated as the superposition of N_p simultaneous nucleon–nucleon collisions.

(ii) A Nucleus–nucleus collision A–B with N_p participating projectile nucleons is approximated as the superposition of N_p simultaneous nucleon–B collisions.

Tables 2 and 3 we present multiplicities and spectrum–weighted moments calculated using DPMJET–II for C–Air collisions. The comparisons in these two Tables with both versions of the superposition model show, that the superposition is only a very rough and unreliable approximation to real nucleus–nucleus collisions.

VII. DPMJET-II AT COSMIC RAY ENERGIES

In [63] we will report about the application of DPMJET-II to study the cosmic ray cascade. Here we give only some general properties of DPMJET-II in this energy range.

A. Important differences between the two-component Dual Parton Model and minijet models

There is no scientific reason, not to call the two-component Dual Parton Model (the two components are the soft pomeron and the hard pomeron or the minijets) also a minijet model. Minijet models too have a soft and a hard component. The reason not to use the term minijet model for DPMJET is connected with the fact, that the name minijet model so far was only used for models which use a critical pomeron with an intercept of exactly one. In such a minijet scheme, it is then claimed, all the rise of the cross sections with energy is due to the rise of the minijet cross sections. This is not so in our model, therefore we avoid to use the name minijet model.

The supercritical pomeron was used in the two-component DPM from the beginning [4], while the so called minijet models use the critical pomeron with $\alpha(0) = 1$ from Durand and Pi [64] over Gaisser and Halzen [65] , SIBYLL [66] up to HIJING [67].

There are important differences which result from this different approach:

(i)Both kinds of models determine the free parameters of their model in a fit to total, inelastic and elastic cross sections. Both models obtain acceptable fits, we have reported even about the fits using a critical pomeron elsewhere [8], but of course, if at the end of the fit we treat the pomeron intercept $\alpha(0)$ as a free parameter instead to fix it to $\alpha(0) = 1$, the fit improves and in all situations (fits using different parton structure functions to calculate the minijet cross sections) we obtain the intercept larger than 1. namely $\alpha(0) \approx 1.07$. These better fits to the data are our main argument for the continuing presence and even rise of soft hadron production at the highest

energies.

(ii)Due to these different starting points the chain structure of the models differ: In both models we have a pair of soft valence–valence chains (resulting from cutting one soft pomeron) and in both models we have minijets. Only in the two component Dual Parton Model we have in addition soft sea–sea chains with soft sea quarks at their ends. The number of these chains increases with energy and a substantial part of the rise of the multiplicity and rapidity plateau results from this mechanism.

(iii)The x–distributions of soft sea quarks are determined by the Regge behaviour, which is for soft sea as well as valence quarks like $1/\sqrt{(x)}$. The minijets are calculated from the deep inelastic structure functions with (depending on the parametrization for the structure functions used) a behaviour like $1/x$ or $1/x^{1.5}$. In the Dual Parton Model the Feynman x_F distributions resulting from fragmenting valence chain ends (which dominate at small energy) and from fragmenting soft sea chain ends do not differ, this is the source of the excellent Feynman scaling and the nearly energy independent spectrum weighted moments. In the minijet models all chains except the single valence chain pair, which dominates at low energy, are minijets with the much softer x–distribution. Therefore in these models Feynman scaling is more strongly violated and the spectrum weighted moments decrease with the collision energy. The rise of the minijet component in the Dual Parton Model leads of course to the same effect, this effect is however smaller, since not all of the rise of particle production is due to the minijets.

B. Spectrum weighted moments

In Table 4 we present spectrum weighted moments Z_π and Z_K according to DPMJET–II in p–p and p–Air collisions and inelasticities for the leading baryon K_{ln} (K_{ln} is defined as the average energy fraction carried by the single most energetic baryon in each event). We find, as explained already in the last Section, Z_π and Z_K moments rather constant with the collision energy. The moments for p–Air collisions

are smaller than for p–p collisions. This decrease is connected with the $\alpha(x_F)$ behaviour as given in Fig. 25. The inelasticities K_{ln} decrease with energy, this decrease will be discussed in the next Section.

In Tables 5 and 6 we give Z_π and Z_K moments in π^+–p, π^+–Air, K^+–p and K^+–Air collisions. Again, the moments for the produced particles are rather constant with rising energy, while the moments for the leading hadrons decrease systematically with rising energy.

In Table 7 we compare the Z_π and Z_K moments calculated with DPMJET–II in p–Air collisions with the ones resulting from HEMAS [68] and SIBYLL [66]. The agreement of the moments, especially the ones from DPMJET–II and from SIBYLL is certainly much better, than expected from the errors of the experimental data used to tune the parameters of the models.

C. Inelasticities

In Table 4 we presented already the inelasticities K_{ln} for leading baryons as calculated from DPMJET–II for p–p and p–Air collisions. In Table 8 we present the inelasticities K_h in p–Air collisions calculated fron DPMJET–II for the most important secondaries as function of the energy. We repeat here, since the definitions of inelasticities differ in the literature, our inelasticities K_h are defined as the fraction of the laboratory energy carried away in the average by secondary hadrons of kind h.

We observe in Tables 4 and 8 a decrease if the inelasticities of all leading baryons (p, n and Λ) while the inelasticities of all newly produced kinds of hadrons increase with energy. A large part of this effect is due to the diffractive component.

In the two–component Dual Parton Model [10] we obtain inelastic cross sections rising with energy like $\log^2 s$. The single diffractive cross sections , where the experimental data are not really a guidance, seem in the model at high energy to approach an energy independent value. A similar result was obtained recently by Gotsman, Levin and Maor [69]. The double diffractive cross sections in the model behave simi-

larly.

The leading hadron inelasticities are particularly large in diffractive events. If the relative fraction of diffractive events decreases with rising energy, we expect a decrease of the inelasticities of the leading hadrons and a corresponding increase of the inelasticities of produced hadrons as found in Table 8 . In this situation, we stress the importance of experimentasl measurements of the hadron production in the fragmentation region , including the measurement of diffractive cross sections at the highest available accelerator energies at the Fermilab Collider. Without such experimental data we have only the models to extrapolate into the Cosmic Ray energy region.

D. Upper energy limit for DPMJET–II calculations

Presently DPMJET–II is able to run up to energies of approximately 10^{18} eV in the lab system. There are trivial reasons for this limit (dimensions in fields to be defined during initialization), which could result in a failure to run at higher energies. Such problems would be easy to solve, but there are besides these trivial reasons physical reasons, that the code should not be used at higher energies.

The most important of these reasons is connected with the minijet component. The way in which the minijet component is implemented in DTUJET93 and DPMJET–II is described in Ref. [10]. This method is expected to break down for structure functions with $1/x^{1.5}$ singularities (for sea quarks and gluons) at higher energies. These structure functions are suggested by the first measurements at the HERA accelerator. For the older structure functions with a $1/x$ singularities, it would be rather straightforward to define the minijet component at higher energies, but this might not correspond to the correct physics. There are certainly ideas, how to extend the treatment of the minijet component up to higher energies, but this would be connected with large and extensive modifications in the model.

VIII. SUMMARY

The event generator DPMJET–II based on the Dual Parton Model has become a valid alternative to models like HEMAS [68], and SIBYLL [66] to simulate the high energy hadron–hadron, hadron–nucleus and nucleus–nucleus collisions within a Cosmic Ray cascade code.

The excellent Feynman scaling found with DPMJET in large parts of the x_F–region in hadron–hadron and hadron–nucleus collisions gives us the confidence, that accelerator data on Feynman x_F–distributions in the projectile fragmentation region are indeed very relevant for applications in the Cosmic Ray energy region.

The model provides hadron–hadron total, inelastic, elastic and diffractive cross sections consistent with accelerator data. The hadron–Air cross sections derived from this are consistent with hadron–Air cross sections extracted from Cosmic Ray experiments. The model provides also all the necessary cross sections to study nucleus–nucleus collisions in the Cosmic Ray cascade.

As a consequence from the excellent Feynman scaling in the model we find spectrum–weighted moments Z_π and Z_K for hadron–Air collisions, which remain rather constant with increasing collision energy, in contrast to the behaviour of other models, where these moments decrease more strongly with energy. These moments for h–Air collisions are however smaller than the corresponding moments in hadron–hadron collisions.

The fraction of the primary energy carried by the leading particles in the collision decreases with energy and with the mass of the target nuclei. A large part of this decrease is due to the decreasing fraction of diffractive (single diffractive and double diffractive) events with rising energy and rising target mass.

The model incorporates the Cronin effect and shows a stong seagull effect. Correspondingly the average transverse momenta $< p_\perp >$ rise with the collision energy (mainly due to the rise of the minijet production cross section), with the mass of the

nuclear target and projectile and with rising Feynman x_F.

It is important, that the model is able to give a good description of hadron production in nucleus–nucleus collisions. Due to the large fraction of nuclei in primary Cosmic Rays nucleus–Air collisions are of great importance in the Cosmic Ray cascade. It has been shown, that these collisions in the Dual Parton Model differ from what is expected in simple approximations like different superposition models.

Finally, we find , in agreement to what is known from accelerator experiments significant enhancements of strange hadron production with the collision energy, with the transverse momentum, with the secondary multiplicity of the collision and with the mass of the nuclear projectils and targets.

Acknowledgements

The author acknowledges the collaboration with P.Aurenche, F.Bopp, A.Capella, R.Engel, A.Ferrari, H.J.Möhring, C.Pajares, D.Pertermann, S.Roesler, P.Sala and J.Tran Thanh Van on different aspects of the Dual Parton model. The collaboration with G.Battistoni and C.Forti on different aspects of the Cosmic Ray application of the model was essential for the progress of the studies presented. The Author achnowledges the hospitality of Prof. L.Mandelli in Milano and Prof. E.Iarocci and Prof. M.Spinetti in Frascati , where the presented calculations were performed and he thanks INFN for supporting these studies.

REFERENCES

[1] G. F. Chew and C. Rosenzweig, *Nucl. Phys.* B104(1976)290.

[2] C. Hong-Mo, J. E. Paton and T. Sheung Tsun, *Nucl. Phys.* B86(1975)470.

[3] A. Capella, U. Sukhatme,Chung I Tan and J. Tran Thanh Van, *Phys. Rep.* 236(1994)225.

[4] A. Capella, J. Tran Thanh Van and J. Kwiecinski, *Phys. Rev. Lett.* 58(1987)2015.

[5] P. Aurenche, F. W. Bopp, A. Capella, J. Kwiecinski, M. Maire, J. Ranft and J. Tran Thanh Van, *Phys. Rev.* D45(1992)92.

[6] F. W. Bopp, A. Capella, J. Ranft and J. Tran Thanh Van, *Z. Phys.* C51(1991)99.

[7] F. W. Bopp, D. Pertermann and J. Ranft, *Z. Phys.* C54(1992)683.

[8] R. Engel, F. W. Bopp, D. Pertermann and J. Ranft, *Phys. Rev.* D46(1992)5192.

[9] S. Roesler, R. Engel and J. Ranft, *Z. Phys.* C59(1993)481.

[10] F. W. Bopp, D. Pertermann, R. Engel and J. Ranft,, *Phys. Rev.* D 49(1994)3236.

[11] B. L. Combridge, J. Kripfganz and J. Ranft, *Phys. Lett.* 70B(1977)234.

[12] K. Hahn and J. Ranft, *Phys. Rev.* D41(1990)1463.

[13] A.Capella and J.Tran Thanh Van , *Z. Phys.* C 10(1981)249.

[14] A.B.Kaidalov and O.I.Piskunova , *Z. Phys.* C 30(1986)145.

[15] A. D. Martin, R. G. Roberts and W. J. Stirling, *Phys. Rev.* D47(1993)867.

[16] C.-C. J.Botts et al., to be published in Phys. Lett. B, 1993.

[17] E.M.Levin, to be publ. in Proc. of Aachen Conf. "QCD – 20 years later" , 1992.

[18] H.-C. Abt, T. et al., DESY preprint DESY 93–117, subm. to Nucl.Phys.B,, 1993.

[19] J. Kwiecinski, A. D. Martin, R. G. Roberts and W. J. Stirling, *Phys. Rev.* D42(1990)3645.

[20] J. Ranft and S. Ritter, *Z. Phys.* C 20(1983)347.

[21] J. Ranft and S. Ritter, *Z. Phys.* C 27(1985)569.

[22] H.-J. Möhring, J. Ranft and S. Ritter, *Z. Phys.* C 27(1985)419.

[23] J. Ranft , *Phys. Lett.* 188B(1987)379.

[24] J. Ranft , *Z. Phys.* C 43(1989)439.

[25] V.S.Barashenkov and V.D.Toneev, High-energy hadron-nucleus and nucleus-nucleus interactions (in russian), *Moscow* Atomisdat(1972).

[26] H.W. Bertini, *Phys. Rev.* 131(1963)1801.

[27] L. Landau and I. Pomeranchuk, *Dokl. Akad. Nauk SSR* 92(1953)535, 734.

[28] L. Stodolski, *Proc. Vth Intern. Colloquium on Multiparticle Reactions* Oxford(1975)577.

[29] J. Ranft , *Phys. Rev.* D 37(1988)1842.

[30] H.-J. Möhring and J. Ranft, *Z. Phys.* C52(1991)643.

[31] I.Kawrakow, H.–J.Möhring and J.Ranft, *Z. Phys.* C56(1992)115.

[32] H.–J. Möhring, J. Ranft, A. Capella and J. Tran Thanh Van, *Phys. Rev.* D47(1993)4146.

[33] J. Ranft, A. Capella and J. Tran Thanh Van, *Phys. Lett.* B320(1994)346.

[34] S.Yu.Shmakov,V.V.Uzhinskii andA.M.Zadoroshny, *Comp.Phys.Comm.* 54(1989)125.

[35] S. Ritter, *Comput. Phys. Commun.* 31(1984)393.

[36] J. Ranft and S. Ritter, *Acta Phys. Pol. B* 11(1980)259.

[37] K. Hänssgen and S. Ritter, *Comput. Phys. Commun.* 31(1984)411.

[38] T. Sjöstrand, CERN Report CERN-TH.6488/92, 1992.

[39] J. W. Cronin et al., *Phys. Rev.* D 11(1975)3105.

[40] H. R. Schmidt and J. Schukraft, GSI–preprint GSI–92–19 1992.

[41] S.Roesler and J.Ranft, *Z. Phys.* (1993).

[42] I.Kawrakow, H.–J.Möhring and J.Ranft, *Phys. Rev.* D47(1993)3849.

[43] H.-J. Möhring and J. Ranft, *Z. Phys.* C52(1991)643.

[44] M.Gazdzicki and O.Hansen , *Nucl. Phys.* A 528(1991)754.

[45] M.Adamus et al., EHS–NA22 Collaboration,, *Z. Phys.* C 39(1988)311.

[46] M.Aguilar–Benitez et al., LEBS–EHS Collaboration,, *Z. Phys.* C 50(1991)405.

[47] J.L.Bailly et al., EHS–RCBC–Collaboration,, *Z. Phys.* C 35(1987)309.

[48] T.Kafka et al.,, *Phys. Rev.* D 16(1977)1261.

[49] A.E.Brenner et al.,, *Phys. Rev.* D 26(1982)1497.

[50] H.Kichimi et al., *Phys. Rev.* D 20(1979)37.

[51] J.L.Bailly et al., EHS–RCBC–Collaboration,, *Z. Phys.* C 31(1986)367.

[52] D.Antreasyan et al. , *Phys. Rev.* D 19(1979)764.

[53] T.Alexopoulos et al., E735 Collaboration, Preprint 1992 1992.

[54] N.N.Biswas, E735 Collaboration, in (ed.) W.Yuanfang, L.Linshaou, Proc of the XXI Int. Symp. on Multiparticle Dynamics, World Scientific, Singapore p.308 1992.

[55] R.Castaldi and G.Sanguinetti , *Ann.Rev.Nucl.Part.Sci.* 35(1985)351.

[56] Particle Data Group, *Phys. Rev.* D45(1992)1.

[57] D.S.Barton et al., *Phys. Rev.* D 27(1983)2580.

[58] T.Akesson et al. NA34 Collaboration , *Z. Phys.* C 46(1990)369.

[59] R.Albrecht et al., WA80 Collaborarion, *Z. Phys.* C 47(1990)367.

[60] D.A.Garbutt et al. , *Phys. Lett.* 67B(1977)355.

[61] H.Bialkowska, M.Gazdzicki,W.Retyk and E.Skrzypczak, *Z. Phys.* C 55(1992)491.

[62] P.Scubic et al. , *Phys. Rev.* D 18(1978)3115.

[63] G.Battistoni, C.Forti and J.Ranft, Frascati preprint, to be published 1994.

[64] J. Durand and H. Pi, *Phys. Rev. Lett.* 58(1987)2015.

[65] T.K.Gaisser and F.Halzen , *Phys. Rev. Lett.* 54(1987)1754.

[66] R.S.Fletcher, T.K.Gaisser, P.Lipari and T.Stanev,, Preprint January 1994 1994.

[67] X. N. Wang and M. Gyulassy, *Phys. Rev.* D44(1991)3501.

[68] C.Forti, H.Biloken, B.d'Ettorre Piazzoli, T.K.Gaisser, L.Satta and T.Stanev, *Phys. Rev.* D 42(1990)3668.

[69] E.Gotsman, E.M.Levin and U.Maor, *Phys. Rev.* D 49(1994)4321.

[70] C. Albajar et al., *Nucl. Phys.* B 335(1990)261.

[71] J.L.Bailly et al., EHS–RCBC–Collaboration,, *Z. Phys.* C 35(1987)295.

[72] H.H.Mielke, M.Föller, J.Engler and J.Knapp , *J.Phys.* G 20(1994)637.

FIGURES

FIG. 1. Diagrams and the corresponding cut graphs for the exchange of a) one soft pomeron, b) one hard pomeron, and c) one triple–pomeron (high mass single diffraction). Fig. d) shows one cut pomeron–loop graph (high mass double diffraction). Low mass single diffractive processes (e),(f) and low mass double diffractive processes (g) are introduced via a two–channel eikonal formalism

FIG. 2. Test of Feynman scaling in the production of leading baryons in proton – proton collisions. The Feynman–x distributions were calculated with the Dual Partom Model DPMJET–II.

FIG. 3. Test of Feynman scaling in the production of π^+ in proton –proton collisions. The Feynman–x distributions were calculated with the Dual Partom Model DPMJET–II.

FIG. 4. Comparison of Feynman–x distributions of π^-–mesons produced in proton–proton collisions at 250 GeV. The experimental data are from the EHS–NA22 Collaboration [45]. The calculation uses the Dual Parton Model DPMJET–II.

FIG. 5. Comparison of Feynman–x distributions of positively charged hadrons produced in proton–proton collisions at 250 GeV. The experimental data are from the EHS–NA22 Collaboration [45]. For $x_F \leq -0.4$ the experimental and calculated distributions refer to π^+ only. The calculation uses the Dual Parton Model DPMJET–II.

FIG. 6. Comparison of Feynman-x distributions of π^--mesons produced in proton-proton collisions at 400 and 360 GeV. The experimental data are from the Aguilar-Benitez et al. [46] and from the EHS-RCBC-Collaboration [47]. The data from both experiments agree rather well with each other, in fact most of the data points of [47] are below the [46] data. The calculation uses the Dual Parton Model DPMJET-II.

FIG. 7. Comparison of Feynman-x distributions of π^+-mesons produced in proton-proton collisions at 205 and 175 GeV. The experimental data are from Kafka et al. [48] and from Brenner et al. [49]. The data from both experiments agree rather well with each other. The calculation uses the Dual Parton Model DPMJET-II.

FIG. 8. Comparison of transverse momentum distributions with collider data at $\sqrt{s}$ = 200 GeV. [70] The calculation uses the Dual Parton Model DPMJET-II.

FIG. 9. Comparison of the seagull effect in the reaction p+p$\rightarrow$ h^- +X at 360 GeV. The data are from the EHS-RCBC Collaboration [71]. The calculation uses the Dual Parton Model DPMJET-II.

FIG. 10. Comparison of the seagull effect in the reaction p+p$\rightarrow$ h^+ +X at 360 GeV. The data are from the EHS-RCBC Collaboration [71]. The calculation uses the Dual Parton Model DPMJET-II.

FIG. 11. Comparison of Feynman-x distributions of K^+-mesons produced in proton-proton collisions at 400 GeV. The experimental data are from the LEBC-EHS Collaboration [46]. The calculation uses the Dual Parton Model DPMJET-II.

FIG. 12. Comparison of Feynman–x distributions of Λ–Hyperons produced in proton–proton collisions at 360 and 405 GeV. The experimental data are from the EHS–RCBC–Collaboration [51] and from Kichimi et al. [50]. The calculation uses the Dual Parton Model DPMJET–II.

FIG. 13. Comparison of Feynman–x distributions of K^0_S–mesons produced in proton–proton collisions at 360 and 405 GeV. The experimental data are from the EHS–RCBC–Collaboration [51] and from Kichimi et al. [50]. The calculation uses the Dual Parton Model DPMJET–II.

FIG. 14. Comparison of the seagull effect in the reaction p+p→ Λ +X at 360 GeV. The data are from the EHS–RCBC Collaboration [71]. The calculation uses the Dual Parton Model DPMJET–II.

FIG. 15. The ratio K^+/π^+ as function of the transverse momentum. We compare the results of DPMJET–II at different energies to data of Antreasyan et al.[52].

FIG. 16. K/π–ratios as function of the energy $\sqrt{s}$. Calculated with the Dual Parton Model Monte Carlo code DTUJET–93 [10] with two different values of the parameter s^{qq} characterizing the strange quark probability at the ends of the soft sea–sea chains and semihard chains. The experimental data are collected from the E735–Collaboration at Fermilab [53].

FIG. 17. K/π–ratios as function of the charged plateau. Calculated with the Dual Parton Model Monte Carlo code DTUJET–93 [10] with two different values of the parameter

$s^{'ea}$ characterizing the strange quark probability at the ends of the soft sea–sea chains and semihard chains. The experimental data are from the E735–Collaboration at Fermilab [53].

FIG. 18. Comparison of Feynman–x distributions of π^-–mesons produced in π^+–proton collisions at 250 GeV. The experimental data are from the EHS–NA22 Collaboration [45]. The calculation uses the Dual Parton Model DPMJET–II.

FIG. 19. Comparison of Feynman–x distributions of positively charged hadrons produced in π^+–proton collisions at 250 GeV. The experimental data are from the EHS–NA22 Collaboration [45]. For $x_F \leq -0.4$ the experimental and calculated distributions refer to π^+ only. The calculation uses the Dual Parton Model DPMJET–II.

FIG. 20. Comparison of Feynman–x distributions of π^+– and π^-–mesons produced in π^+–proton collisions at 175 GeV. The experimental data are from Brenner et al. [49] The calculation uses the Dual Parton Model DPMJET–II.

FIG. 21. Comparison of Feynman–x distributions of K^+–, π^+– and π^-–mesons produced in K^+–proton collisions at 175 GeV. The experimental data are from Brenner et al. [49] The calculation uses the Dual Parton Model DPMJET–II.

FIG. 22. The total cross section σ_{p-Air} as function of the collision energy as calculated using the Glauber model in DPMJET–II. The calculation is compared to Cosmic Ray data collected by Mielke et al. [72],

FIG. 23. Test of Feynman scaling in the production of π^+ in proton –Air collisions. The Feynman–x distributions were calculated with the Dual Partom Model DPMJET–II.

FIG. 24. Change of the Feynman–x distributions of protons and π^+–mesons produces in 400 GeV collisions with the mass of the target nucleus. The calculation uses the Dual Parton Model DPMJET–II.

FIG. 25. The nuclear dependence of the Feynman–x distribution in hadron–nucleus collisions is represented in the form $d\sigma/dx_{h-A} = A^{\alpha(x)} d\sigma/dx_{h-h}$. We compare $\alpha(x)$ as determined by Barton et al [57] for pion production at $p_\perp = 0.3$ GeV/c with the DPMJET–II results for all charges hadrons at all values of $p_\perp$.

FIG. 26. Transverse momentum distribution of negatively charged hadrons in p–W collisions at the energy of 200 GeV. We compare the data from the HELIOS Collaboration [58] with the distribution calculated from the Dual Parton Model DPMJET–II.

FIG. 27. Transverse momentum distribution of π^0- mesons in p–Au collisions at the energy of 200 GeV. We compare the data from the WA80 Collaboration [59] with the distribution calculated from the Dual Parton Model DPMJET–II.

FIG. 28. The nuclear dependence ot the $p_\perp$–distributions in proton–nucleus collisions is represented in the $A^{\alpha(p_\perp)}$ form. We compare data from Garbutt et al. [60] for different kinds of produced particles with the results of the Dual Parton Model DPMJET–II for π^+ and K^+.

FIG. 29. The seagull effect as calculated from DPMJET–II for proton–Air collisions at energie between 1 and 1000 TeV.

FIG. 30. Total nucleus–Air cross sections σ_{A-Air} as function of the collision energy as calculated using the Glauber model in DPMJET–II.

Table 1 Comparison of average multiplicities of produced hadrons in proton– proton collisions at 200 GeV. The experimental data are from Ref.[44].

Particle	DPMJET–II	Exp.
n_{ch}	7.66	7.69 ± 0.06
n_-	2.82	2.85 ± 0.03
p	1.34	1.34 ± 0.15
n	0.62	0.61 ± 0.30
π^+	3.17	3.22 ± 0.12
π^-	2.56	2.62 ± 0.06
π^0	3.38	3.34 ± 0.24
K^+	0.28	0.28 ± 0.06
K^-	0.19	0.18 ± 0.05
K^0_S	0.22	0.17 ± 0.01
$\bar{p}$	0.07	0.05 ± 0.02

Table 2 Comparison of average multiplicities calculated in C–Air collisions at different energies with the expectations in two different superposition models. N_p is the average number of projectile nucleons taking part in the inelastic C–Air collision. The energies given are the energy per nucleon!

Energy [TeV]	N_p	$n_{\pi^+}^{C-Air}$	$n_{\pi^+}^{p-p}$	$n_{\pi^+}^{p-Air}$	$N_p n_{\pi^+}^{p-p}$	$N_p n_{\pi^+}^{p-Air}$
10	4.21	27.96	4.35	6.76	18.31	28.46
100	4.45	46.89	6.56	11.35	29.19	50.51
1000	4.69	73.71	9.31	17.45	43.66	81.84

Table 3 Comparison of Z_π–moments calculated in C–Air collisions at different energies with the expectations in two different superposition models. N_p is the average number of projectile nucleons taking part in the inelastic C–Air collision. The energies given are the energy per nucleon!

Energy [TeV]	N_p	Z_π^{C-Air}	Z_π^{p-p}	Z_π^{p-Air}	$N_p Z_\pi^{p-p}$	$N_p Z_\pi^{p-Air}$
10	4.21	.3619	.076	.067	.3200	.2821
100	4.45	.3778	.076	.069	.3382	.3071
1000	4.69	.3872	.076	.068	.3564	.3189

Table 4 Z_π and Z_K moments and leading baryon inelasticities K_{ln} in p–p and p–Air collisions.

Collision	p–p	p–p	p–p	p–Air	p–Air	p–Air
Energy [TeV]	Z_π	Z_K	K_{ln}	Z_π	Z_K	K_{ln}
0.2	0.077	0.0094	0.45			
0.4	0.076	0.0092	0.45			
1	0.076	0.0093	0.45	0.067	0.0098	0.37
10	0.076	0.0092	0.44	0.069	0.0099	0.33
100	0.076	0.0095	0.42	0.068	0.0102	0.31
1000	0.075	0.0093	0.40	0.066	0.0101	0.27

Table 5 Z_π and Z_K moments in π^+–p and π^+–Air collisions.

Collision	π^+–p	π^+–p	π^+–Air	π^+–Air
Energy [TeV]	Z_π	Z_K	Z_π	Z_K
0.2	0.26	0.019	0.24	0.018
1	0.27	0.018	0.23	0.017
10	0.27	0.018	0.23	0.016
100	0.26	0.018	0.21	0.016
1000			0.19	0.015

Table 6 Z_π and Z_K moments in K^+–p and K^+–Air collisions.

Collision	K^+–p	K^+–p	K^+–Air	K^+–Air
Energy [TeV]	Z_π	Z_K	Z_π	Z_K
0.2	0.093	0.171	0.082	0.156
1	0.092	0.181	0.084	0.156
10	0.091	0.188	0.082	0.145
100	0.086	0.183	0.080	0.132
1000			0.076	0.113

Table 7 Comparison of Z_π and Z_K moments in p–Air collisions between DPMJET–II, HEMAS [68] and SIBYLL [66].

	DPMJET	HEMAS	SIBYLL	DPMJET	HEMAS	SIBYLL
Energy [TeV]	Z_π	Z_π	Z_π	Z_K	Z_K	Z_K
1	0.067	0.061	0.072	0.0098	0.0104	0.0073
10	0.069	0.057	0.068	0.0099	0.0113	0.0071
100	0.068	0.056	0.067	0.0102	0.0116	0.0070
1000	0.066	0.056	0.066	0.0101	0.0123	0.0070

Table 8 Inelasticities in p–Air collisions as calculated with DPMJET–II.

Energy [TeV]	K_p	$K_{\bar{p}}$	K_n	K_{π^+}	K_{π^-}	K_{K^+}	K_{K^-}	K_Λ	K_{π^0}
1	0.265	0.011	0.093	0.167	0.138	0.024	0.018	0.023	0.174
10	0.233	0.012	0.091	0.175	0.147	0.025	0.020	0.022	0.181
100	0.212	0.013	0.088	0.179	0.154	0.026	0.022	0.022	0.185
1000	0.189	0.014	0.083	0.185	0.162	0.027	0.023	0.021	0.191
10000	0.168	0.015	0.077	0.190	0.169	0.029	0.025	0.020	0.198
100000	0.152	0.016	0.075	0.194	0.173	0.029	0.026	0.020	0.201

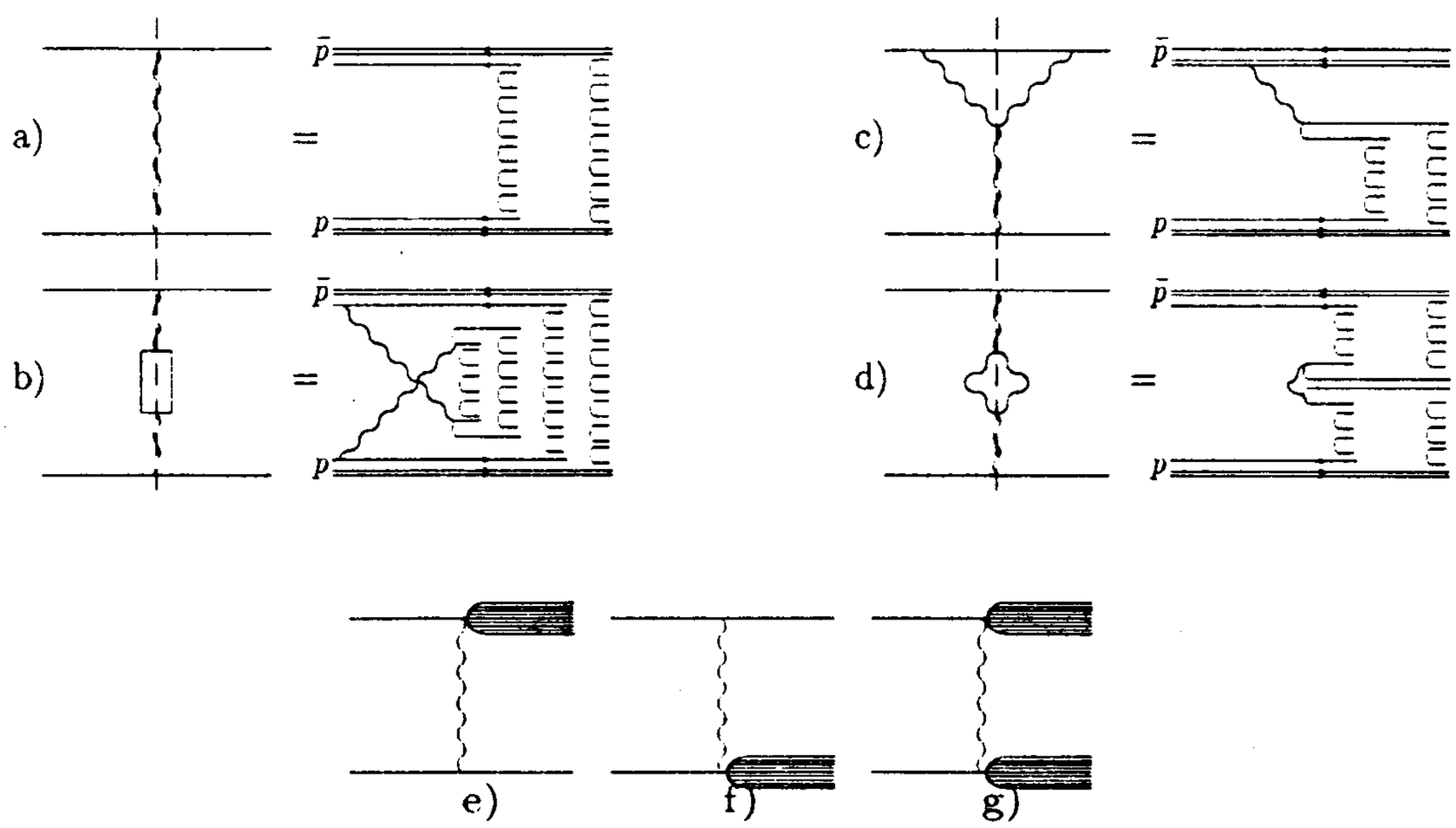

Figure 1.

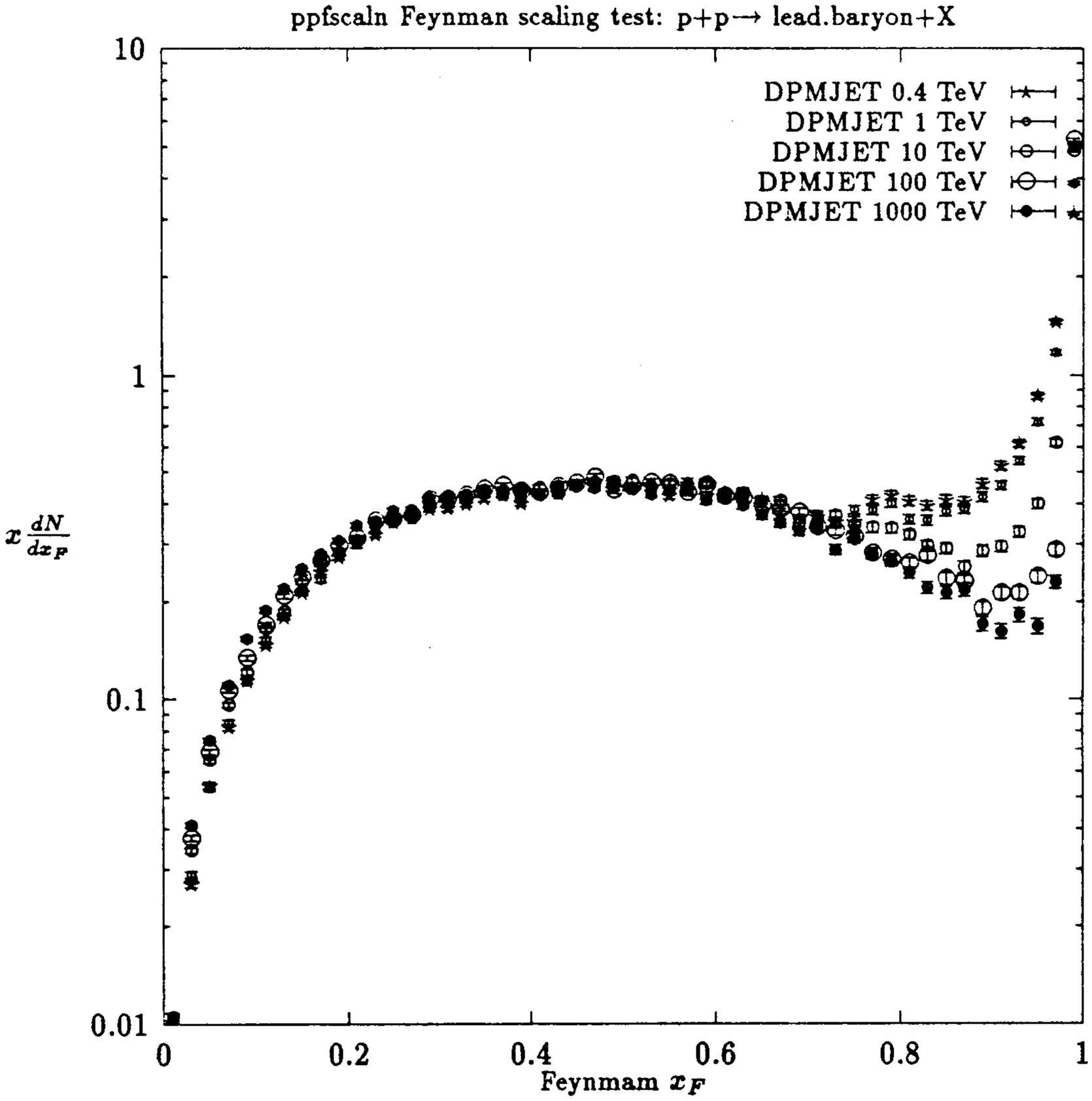
ppfscaln Feynman scaling test: p+p→ lead.baryon+X
DPMJET 0.4 TeV
DPMJET 1 TeV
DPMJET 10 TeV
DPMJET 100 TeV
DPMJET 1000 TeV
$x\frac{dN}{dx_F}$
10
1
0.1
0.01
0
0.2
0.4
0.6
0.8
1
Feynmam x_F

Figure 2.

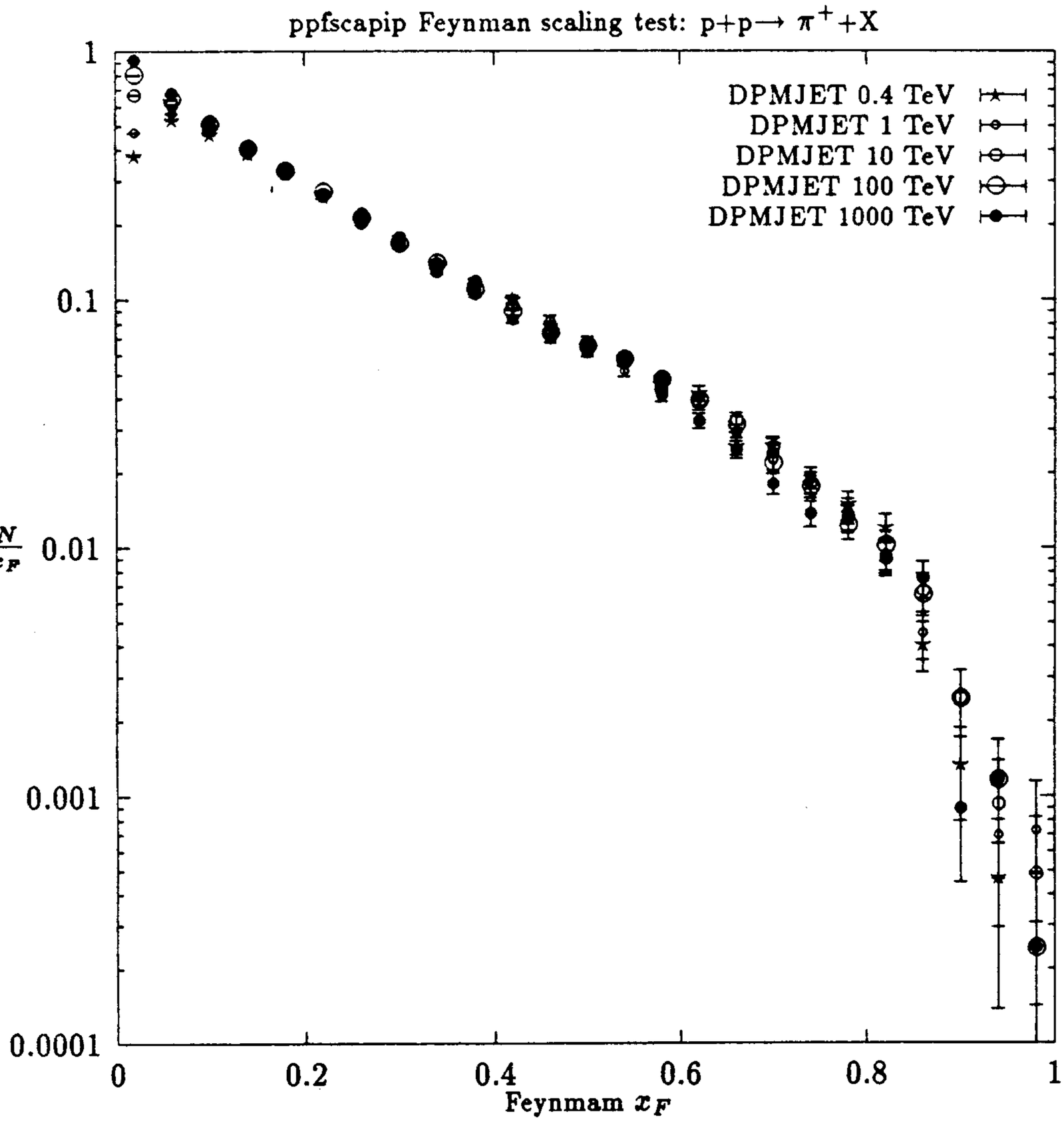
ppfscapip Feynman scaling test: p+p→ π+X
DPMJET 0.4 TeV
DPMJET 1 TeV
DPMJET 10 TeV
DPMJET 100 TeV
DPMJET 1000 TeV
x dN/dx_F
1
0.1
0.01
0.001
0.0001
0
0.2
0.4
0.6
0.8
1
Feynmam x_F

Figure 3.

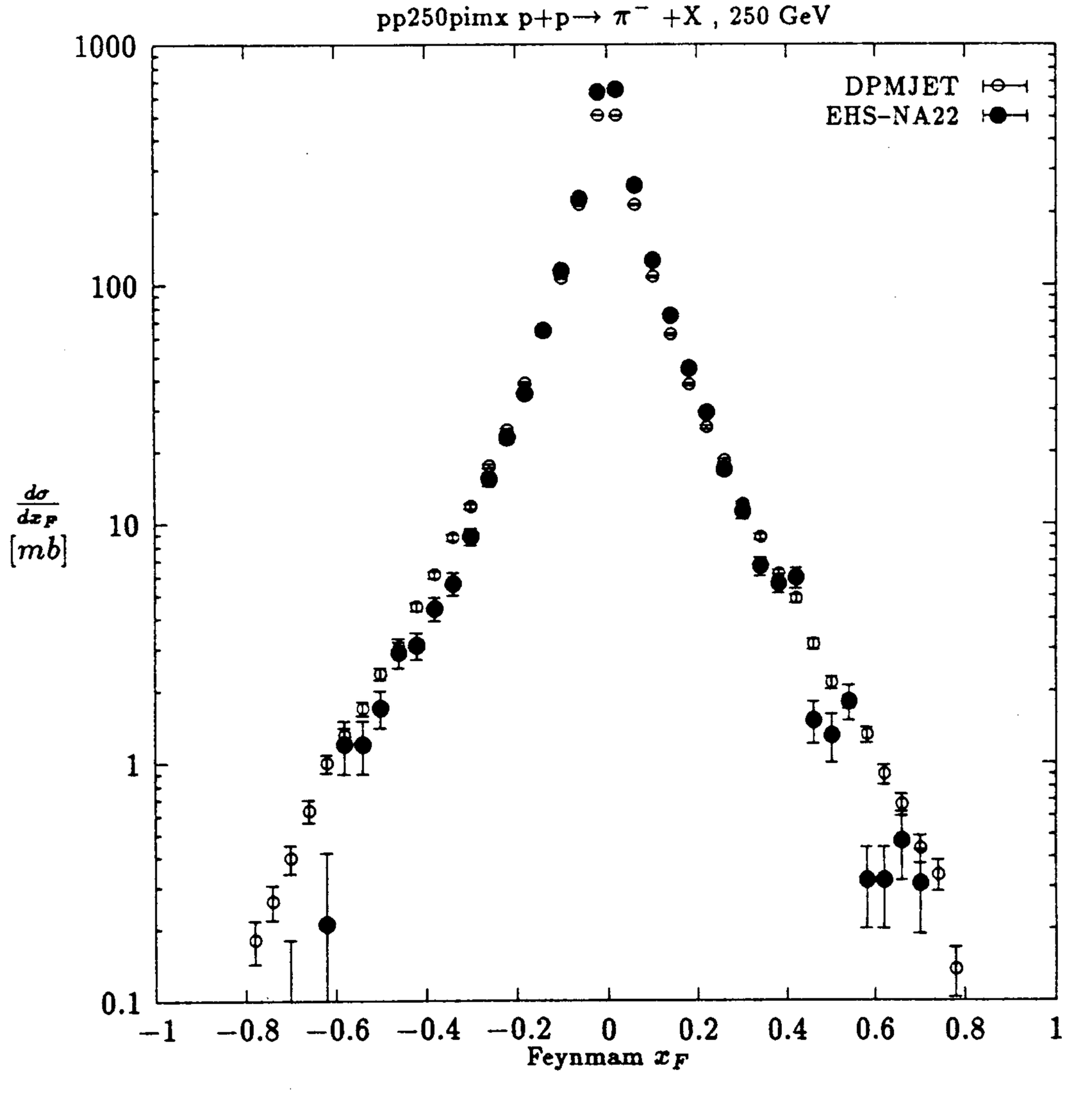
pp250pimx p+p→ π⁻ +X , 250 GeV
DPMJET
EHS-NA22
1000
100
10
1
0.1
dσ/dx_F [mb]
−1
−0.8
−0.6
−0.4
−0.2
0
0.2
0.4
0.6
0.8
1
Feynmam x_F

Figure 4.

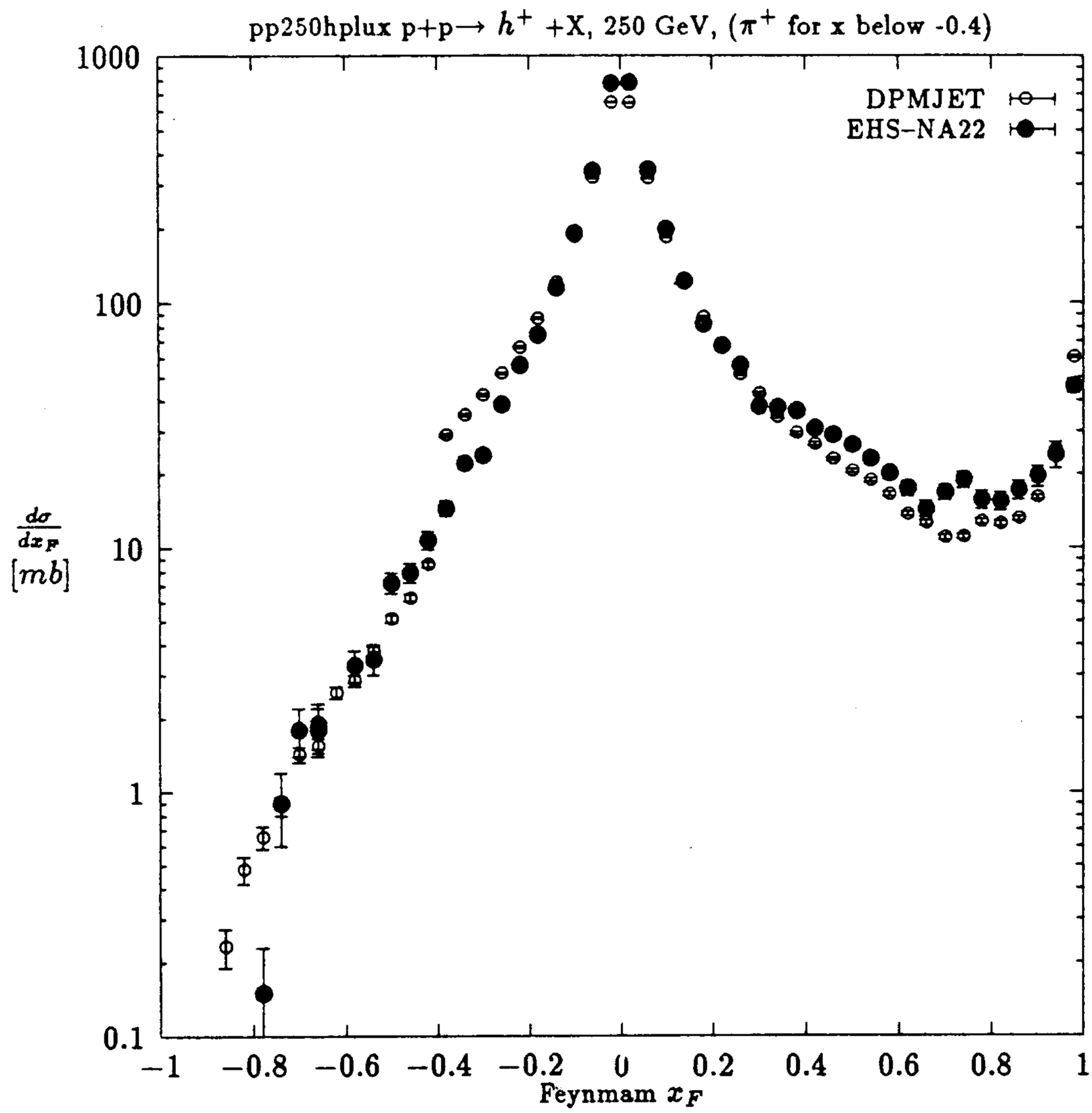
pp250hplux p+p→ h^+ +X, 250 GeV, (π^+ for x below -0.4)
DPMJET
EHS-NA22
$\frac{d\sigma}{dx_F}$ [mb]
1000
100
10
1
0.1
−1
−0.8
−0.6
−0.4
−0.2
0
0.2
0.4
0.6
0.8
1
Feynmam x_F

Figure 5.

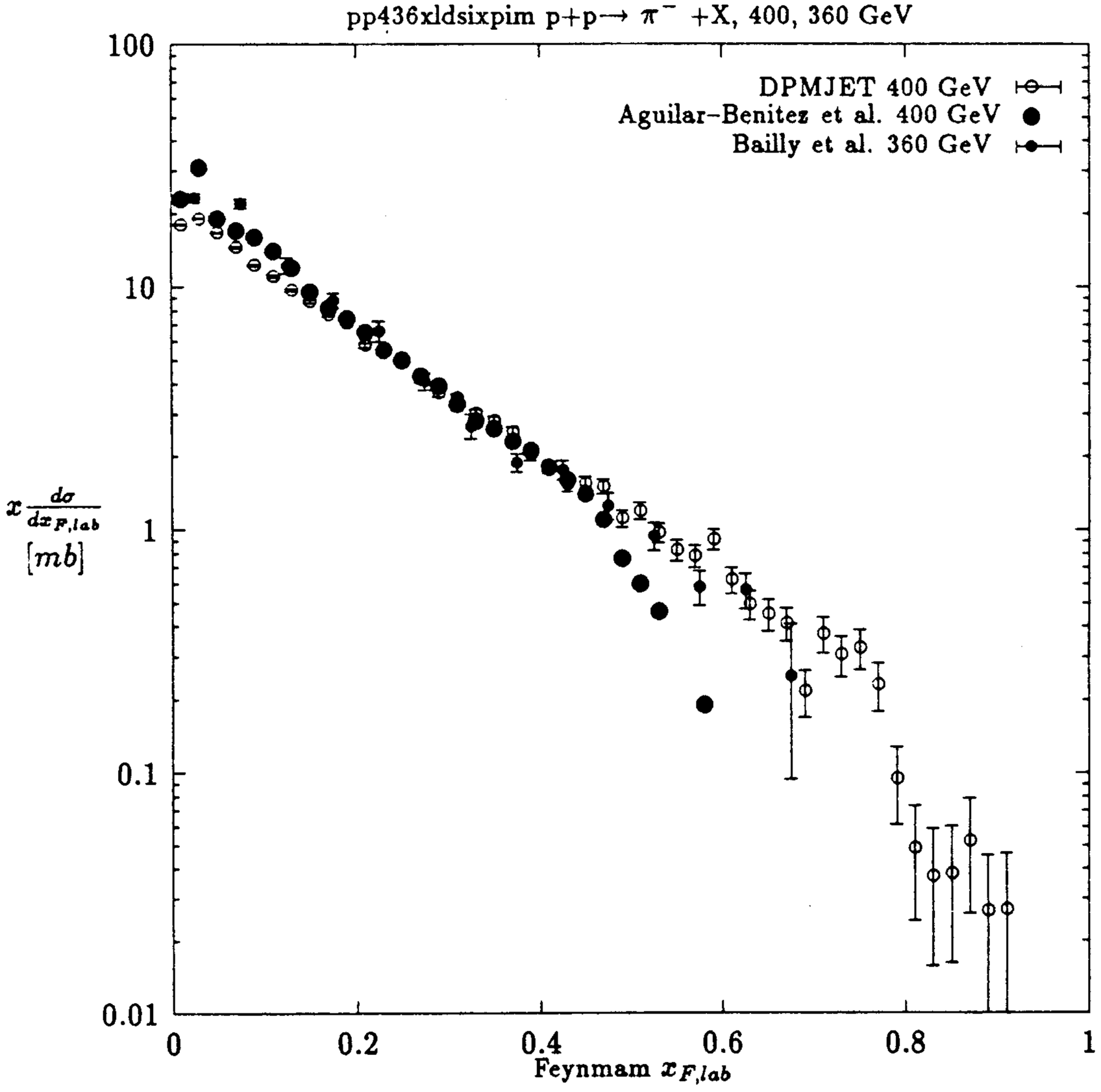
pp436xldsixpim p+p→ π⁻ +X, 400, 360 GeV
DPMJET 400 GeV
Aguilar-Benitez et al. 400 GeV
Bailly et al. 360 GeV
$x\frac{d\sigma}{dx_{F,lab}}$ [mb]
100
10
1
0.1
0.01
0
0.2
0.4
0.6
0.8
1
Feynmam $x_{F,lab}$

Figure 6.

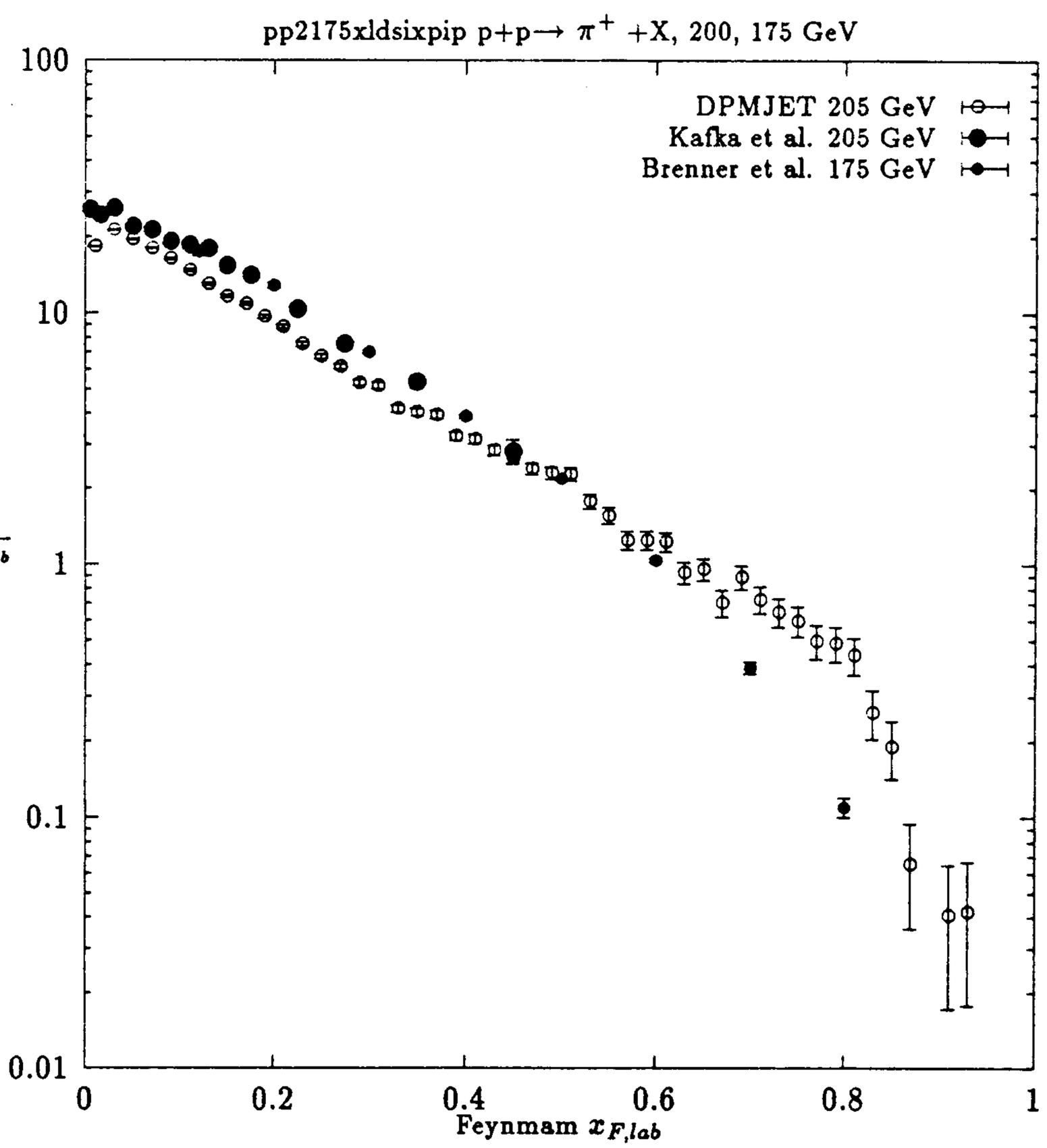
pp2175xldsixpip p+p→ π^+ +X, 200, 175 GeV
DPMJET 205 GeV
Kafka et al. 205 GeV
Brenner et al. 175 GeV
$x \frac{d\sigma}{dx_{F,lab}}$ [mb]
100
10
1
0.1
0.01
0
0.2
0.4
0.6
0.8
1
Feynmam $x_{F,lab}$

Figure 7.

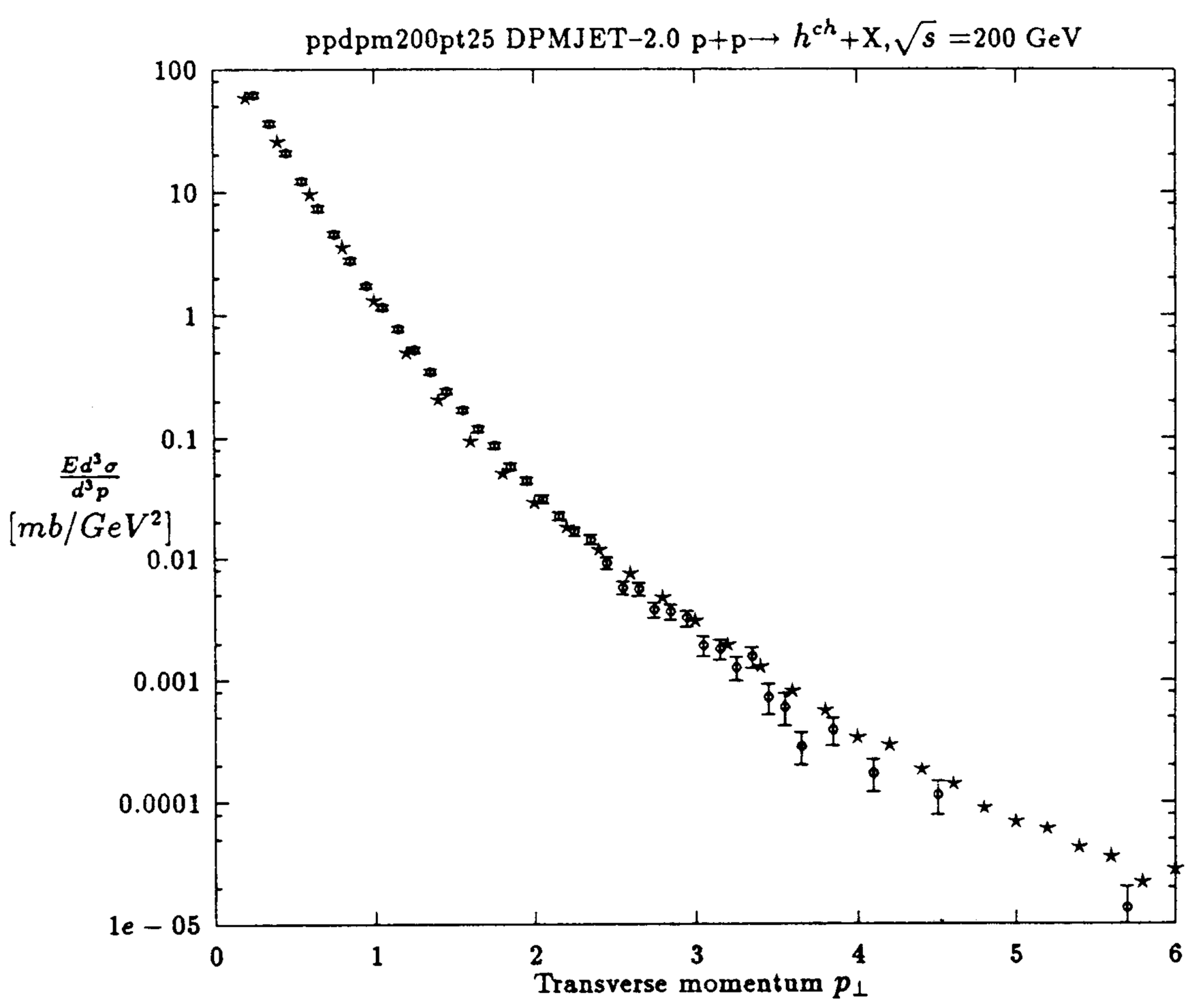
ppdpm200pt25 DPMJET-2.0 p+p⟶ h^{ch}+X,$\sqrt{s}$ =200 GeV
$\frac{Ed^3\sigma}{d^3p}$
$[mb/GeV^2]$
100
10
1
0.1
0.01
0.001
0.0001
1e − 05
0
1
2
3
4
5
6
Transverse momentum $p_\perp$

Figure 8.

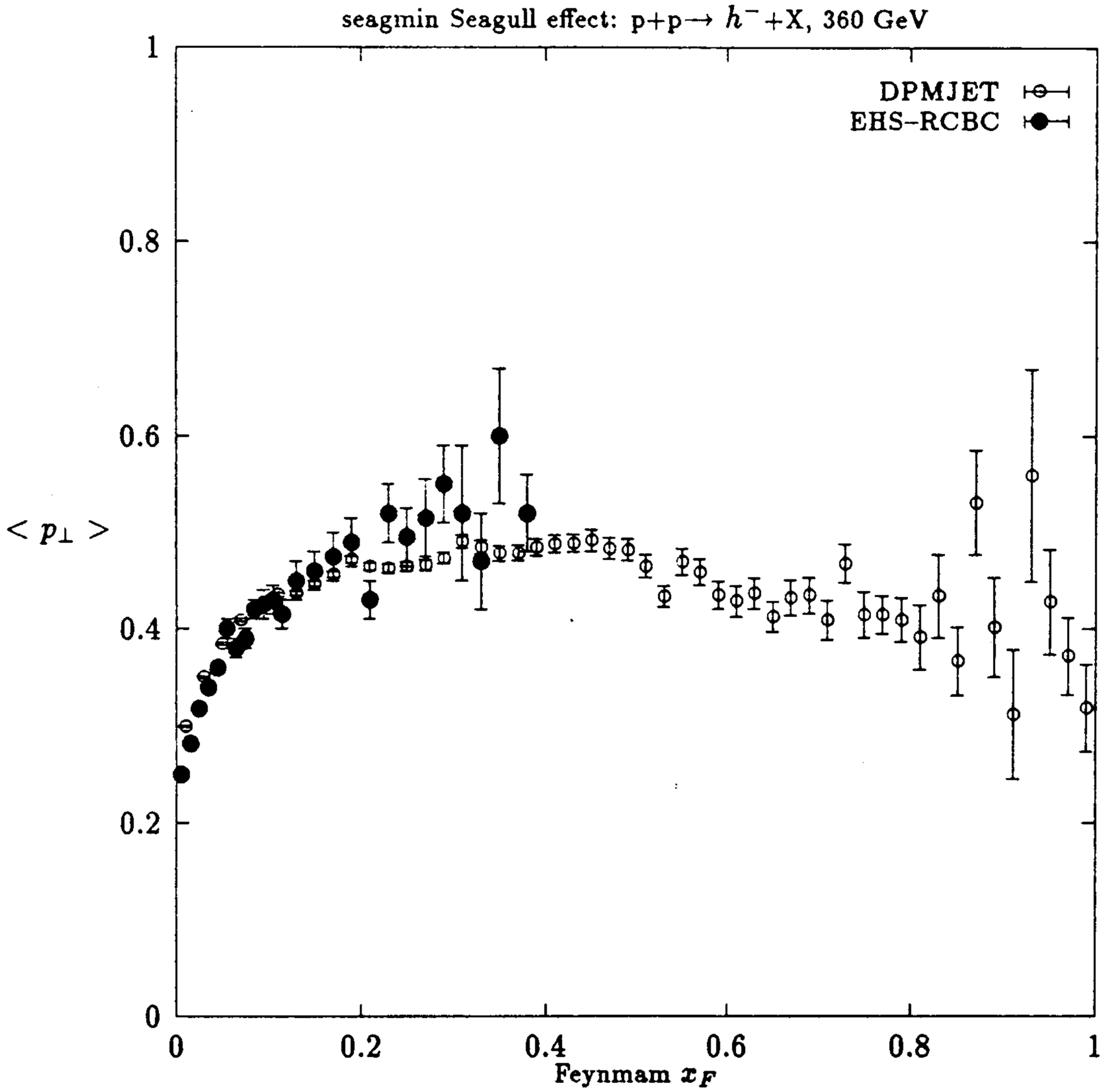
seagmin Seagull effect: p+p→ h^-+X, 360 GeV
DPMJET
EHS-RCBC
$< p_\perp >$
Feynmam x_F
0
0.2
0.4
0.6
0.8
1

Figure 9.

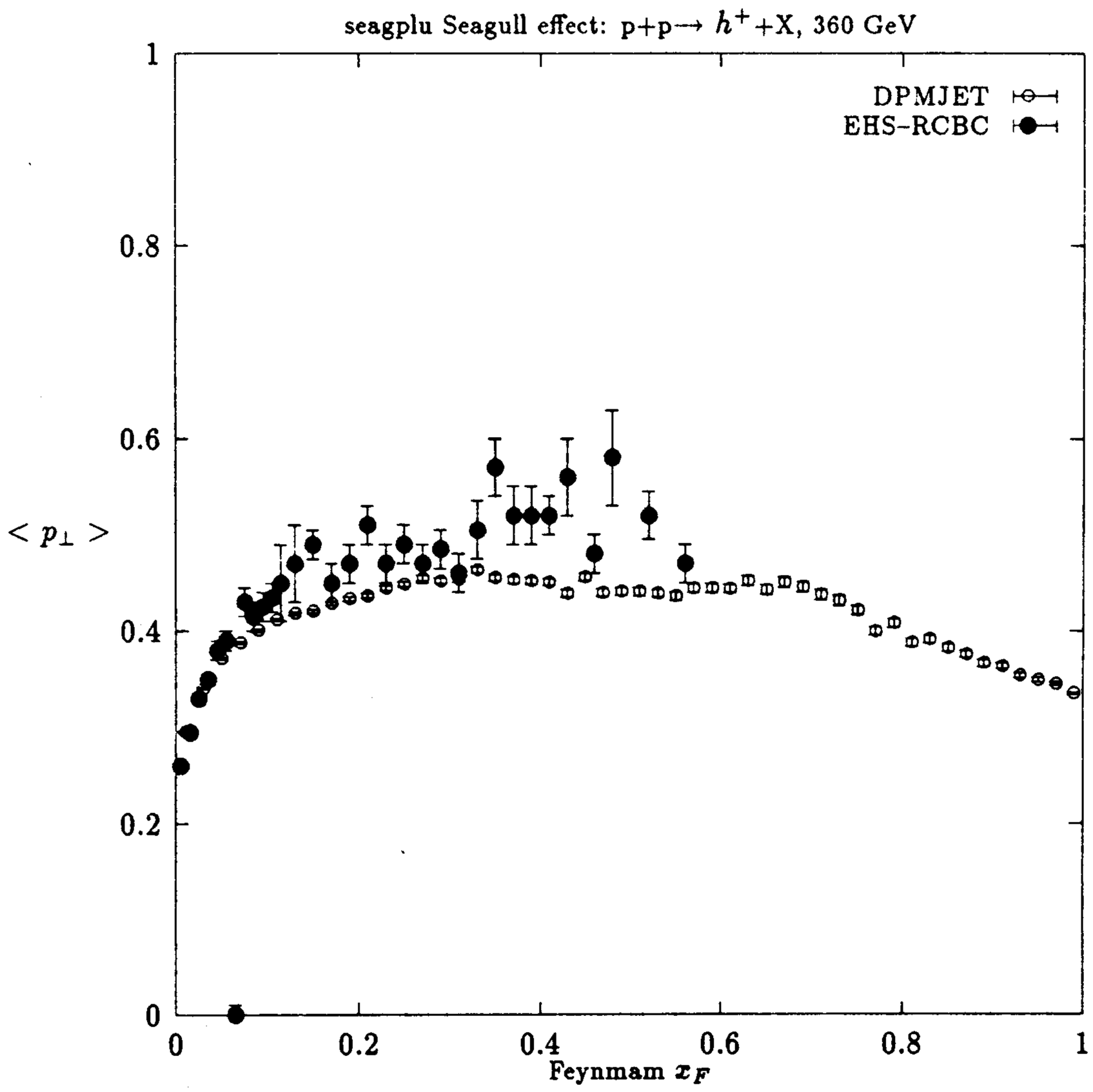
seagplu Seagull effect: p+p→ h^++X, 360 GeV
DPMJET
EHS-RCBC
$< p_\perp >$
Feynmam x_F
0
0.2
0.4
0.6
0.8
1

Figure 10.

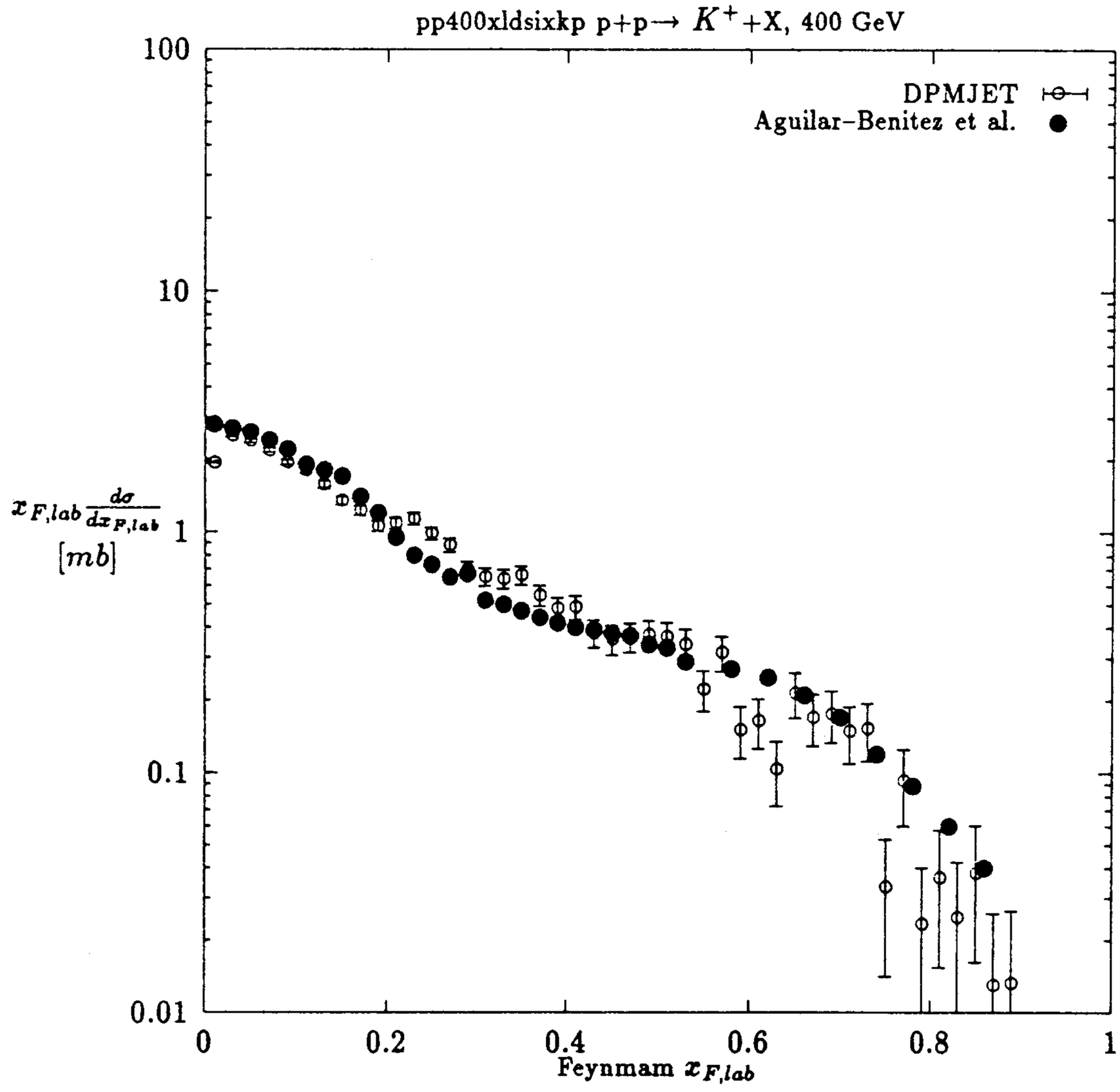
pp400xldsixkp p+p→ K^++X, 400 GeV
DPMJET
Aguilar-Benitez et al.
$x_{F,lab}\frac{d\sigma}{dx_{F,lab}}$ [mb]
100
10
1
0.1
0.01
0
0.2
0.4
0.6
0.8
1
Feynmam $x_{F,lab}$

Figure 11.

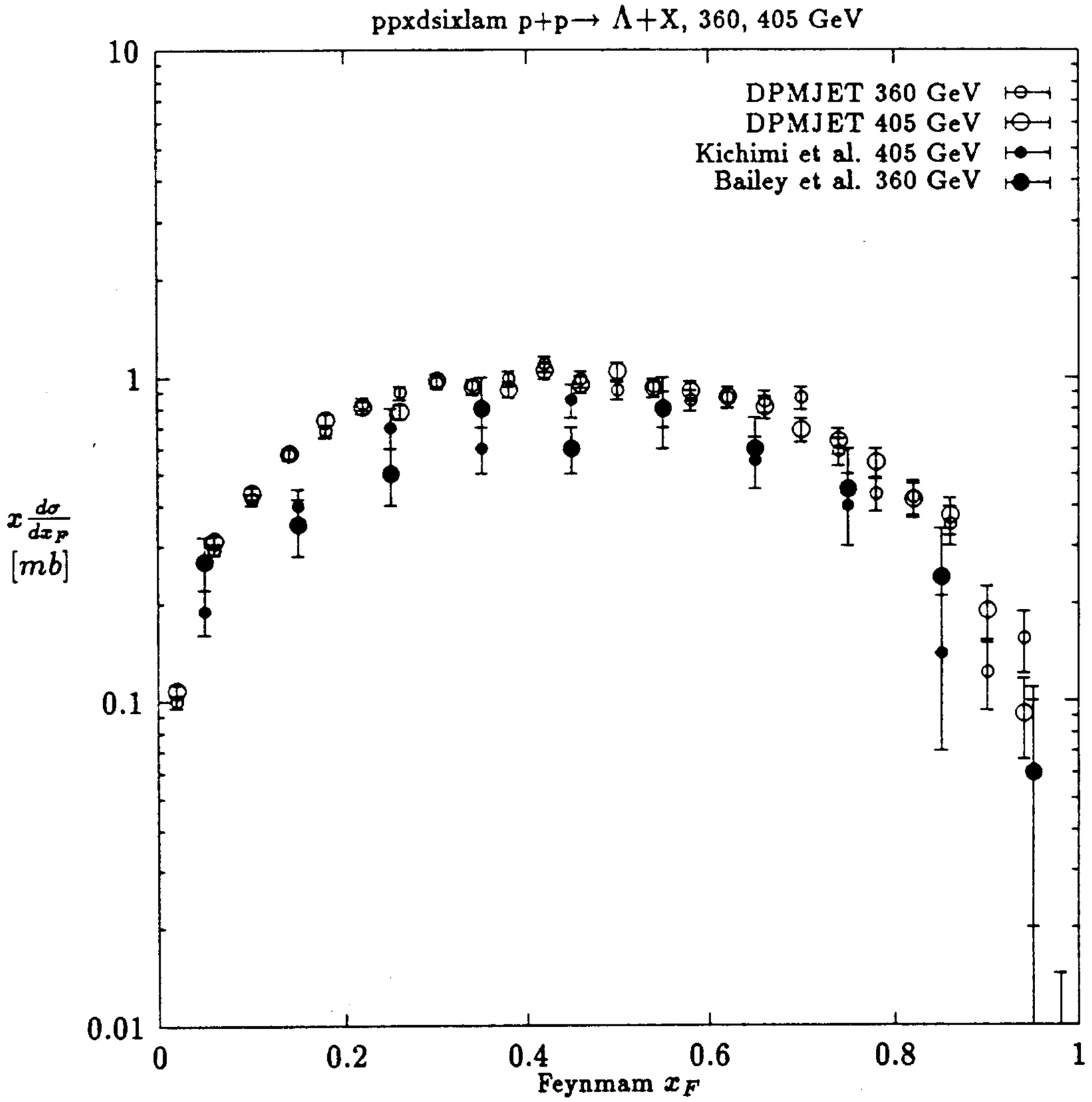
ppxdsixlam p+p→ Λ+X, 360, 405 GeV
DPMJET 360 GeV
DPMJET 405 GeV
Kichimi et al. 405 GeV
Bailey et al. 360 GeV
$x\frac{d\sigma}{dx_F}$ [mb]
10
1
0.1
0.01
0
0.2
0.4
0.6
0.8
1
Feynmam x_F

Figure 12.

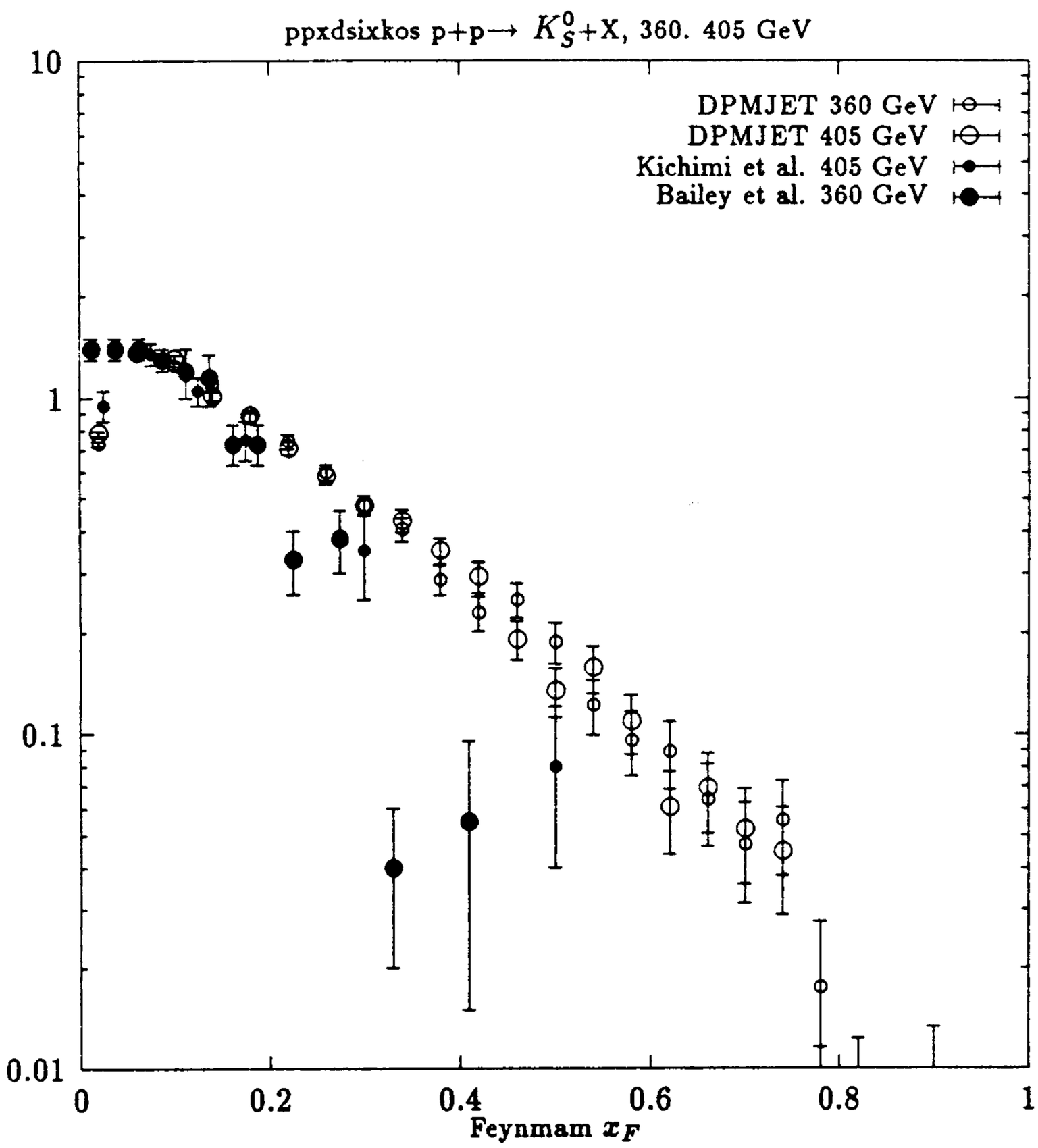
ppxdsixkos p+p→ K^0_S+X, 360. 405 GeV
DPMJET 360 GeV
DPMJET 405 GeV
Kichimi et al. 405 GeV
Bailey et al. 360 GeV
$x\frac{d\sigma}{dx_F}$ [mb]
10
1
0.1
0.01
0
0.2
0.4
0.6
0.8
1
Feynmam x_F

Figure 13.

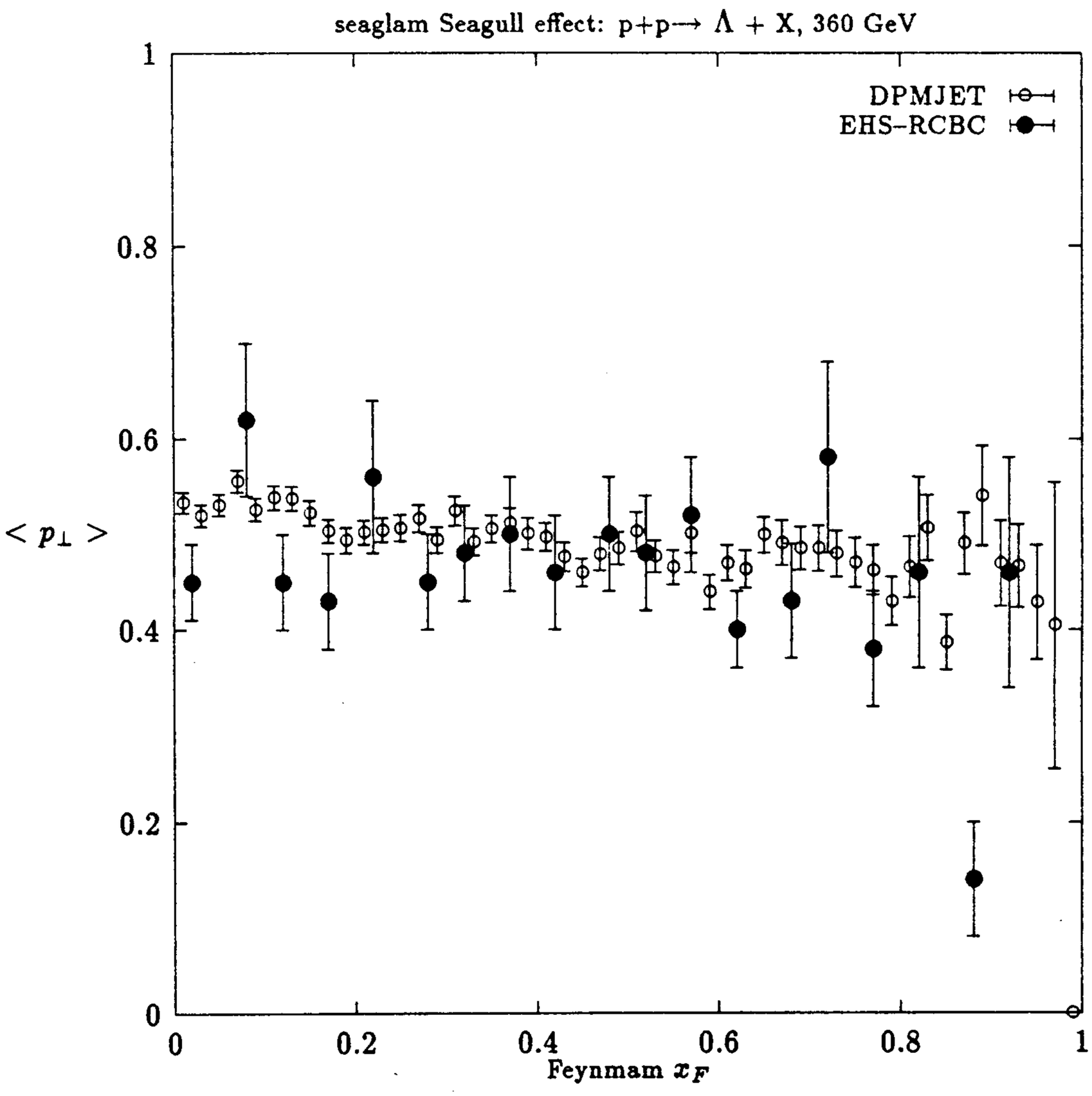
seaglam Seagull effect: p+p⟶ Λ + X, 360 GeV
DPMJET
EHS-RCBC
< $p_\perp$ >
Feynmam x_F
0
0.2
0.4
0.6
0.8
1

Figure 14.

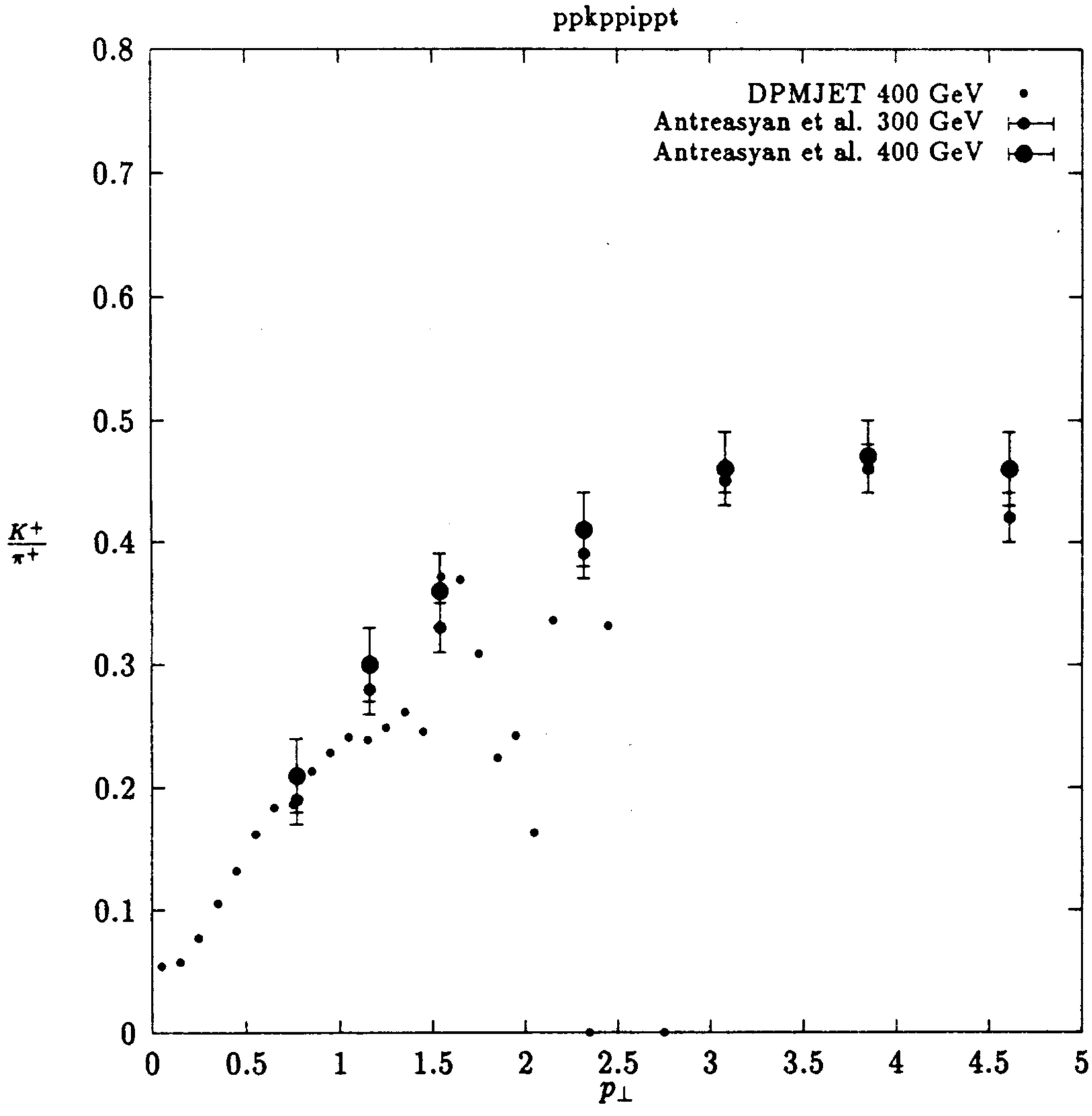
ppkppippt
DPMJET 400 GeV
Antreasyan et al. 300 GeV
Antreasyan et al. 400 GeV
$\frac{K^+}{\pi^+}$
$p_\perp$
0
0.1
0.2
0.3
0.4
0.5
0.6
0.7
0.8
0
0.5
1
1.5
2
2.5
3
3.5
4
4.5
5

Figure 15.

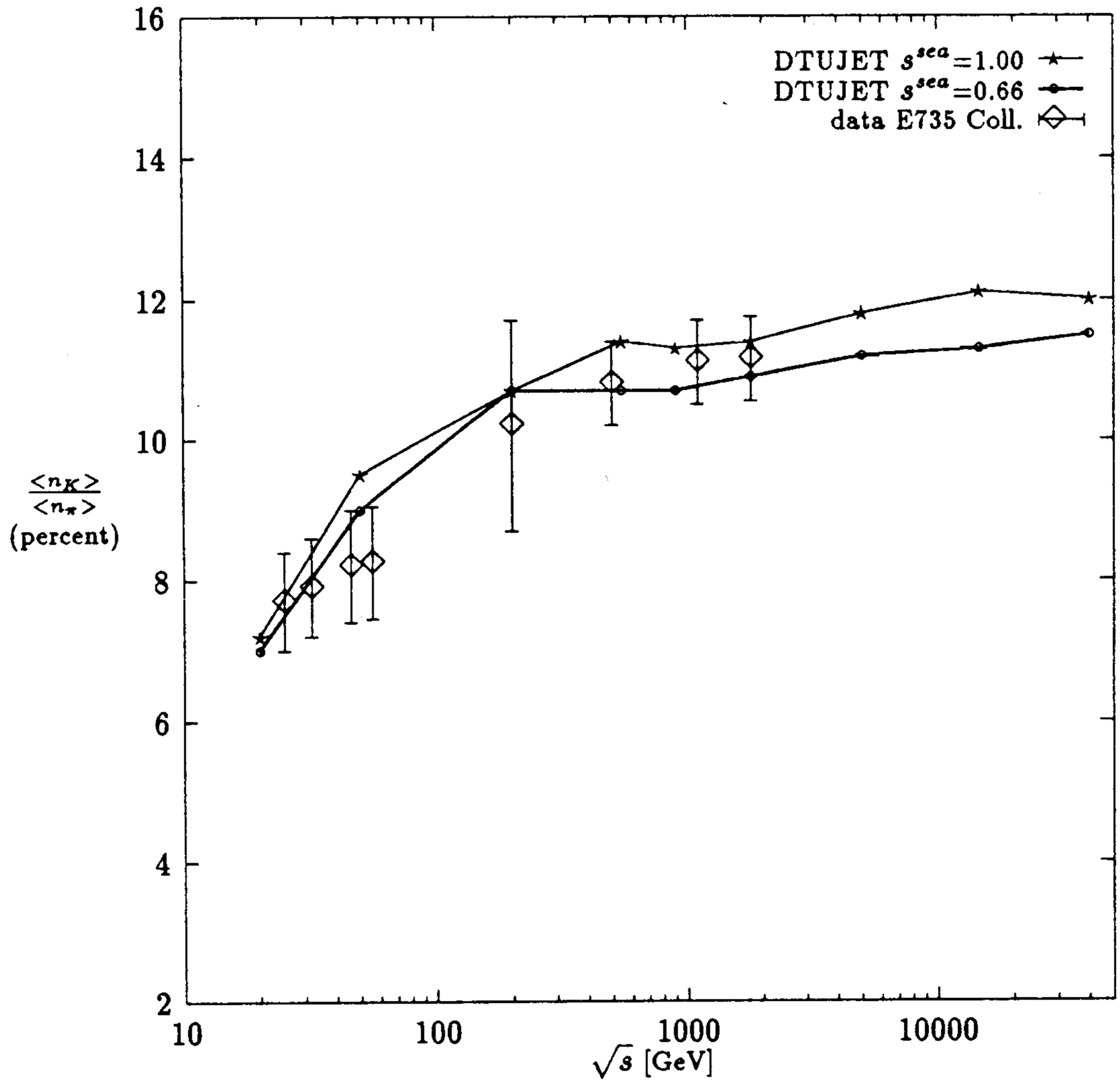
ppkdpi
DTUJET s^{sea}=1.00
DTUJET s^{sea}=0.66
data E735 Coll.
$\frac{<n_K>}{<n_\pi>}$
(percent)
16
14
12
10
8
6
4
2
10
100
1000
10000
$\sqrt{s}$ [GeV]

Figure 16.

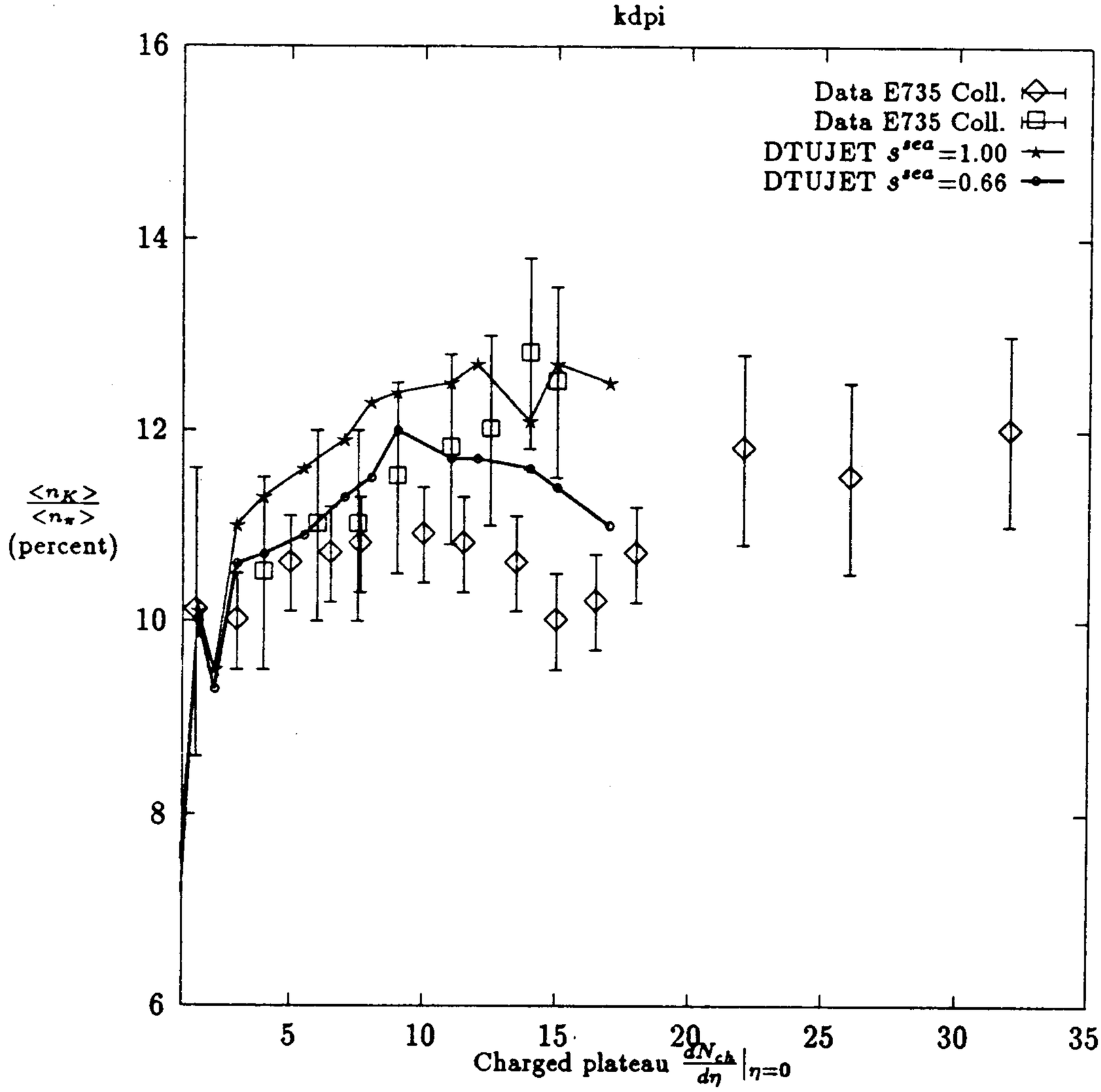
kdpi
Data E735 Coll.
Data E735 Coll.
DTUJET s^{sea}=1.00
DTUJET s^{sea}=0.66
$\frac{<n_K>}{<n_\pi>}$ (percent)
Charged plateau $\frac{dN_{ch}}{d\eta}|_{\eta=0}$
16
14
12
10
8
6
5
10
15
20
25
30
35

Figure 17.

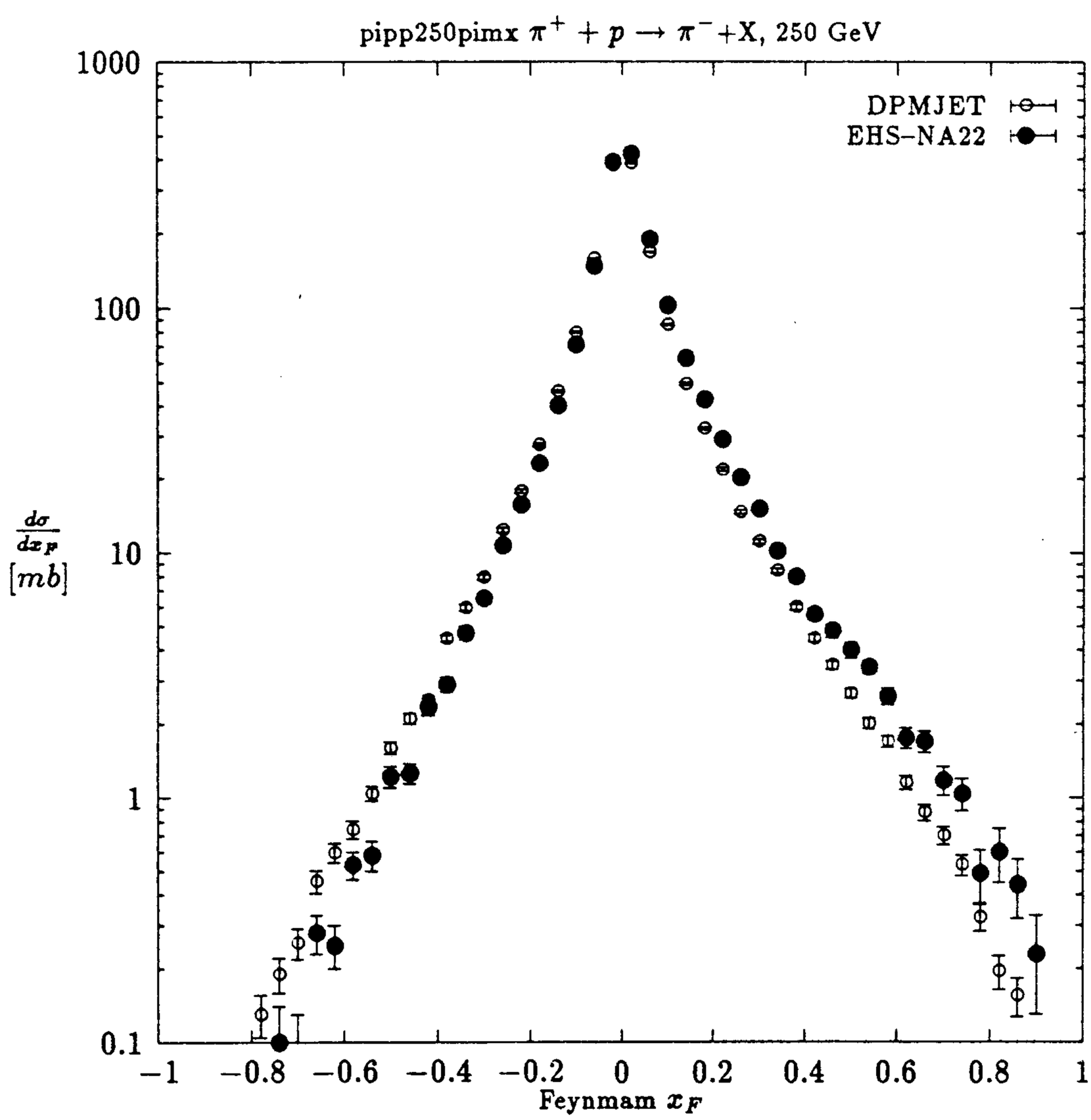
pipp250pimx $\pi^+ + p \rightarrow \pi^-$+X, 250 GeV
DPMJET
EHS-NA22
$\frac{d\sigma}{dx_F}$ $[mb]$
1000
100
10
1
0.1
−1
−0.8
−0.6
−0.4
−0.2
0
0.2
0.4
0.6
0.8
1
Feynmam x_F

Figure 18.

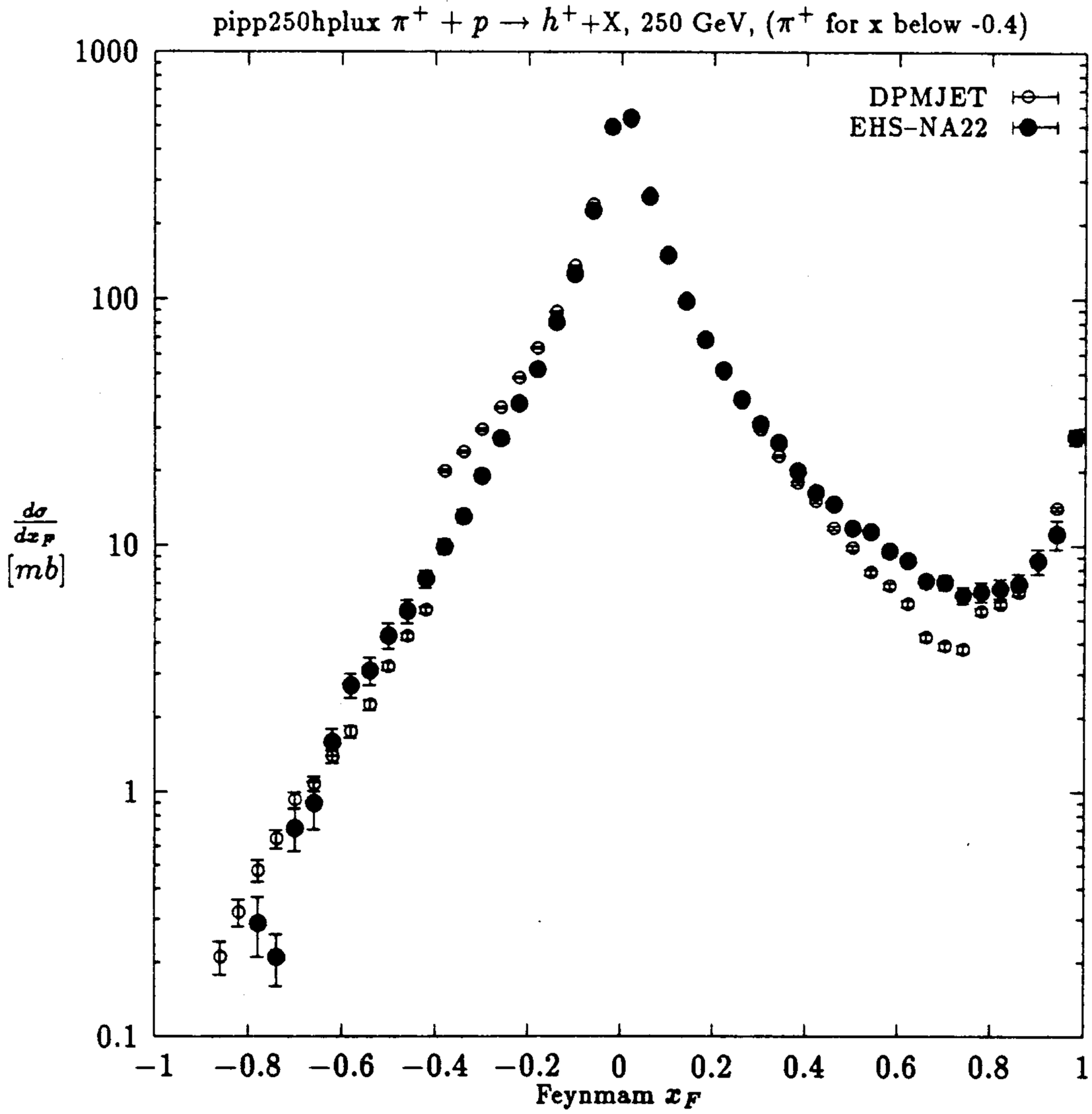
pipp250hplux $\pi^+ + p \rightarrow h^+$+X, 250 GeV, ($\pi^+$ for x below -0.4)
DPMJET
EHS-NA22
$\frac{d\sigma}{dx_F}$ [mb]
1000
100
10
1
0.1
−1
−0.8
−0.6
−0.4
−0.2
0
0.2
0.4
0.6
0.8
1
Feynmam x_F

Figure 19.

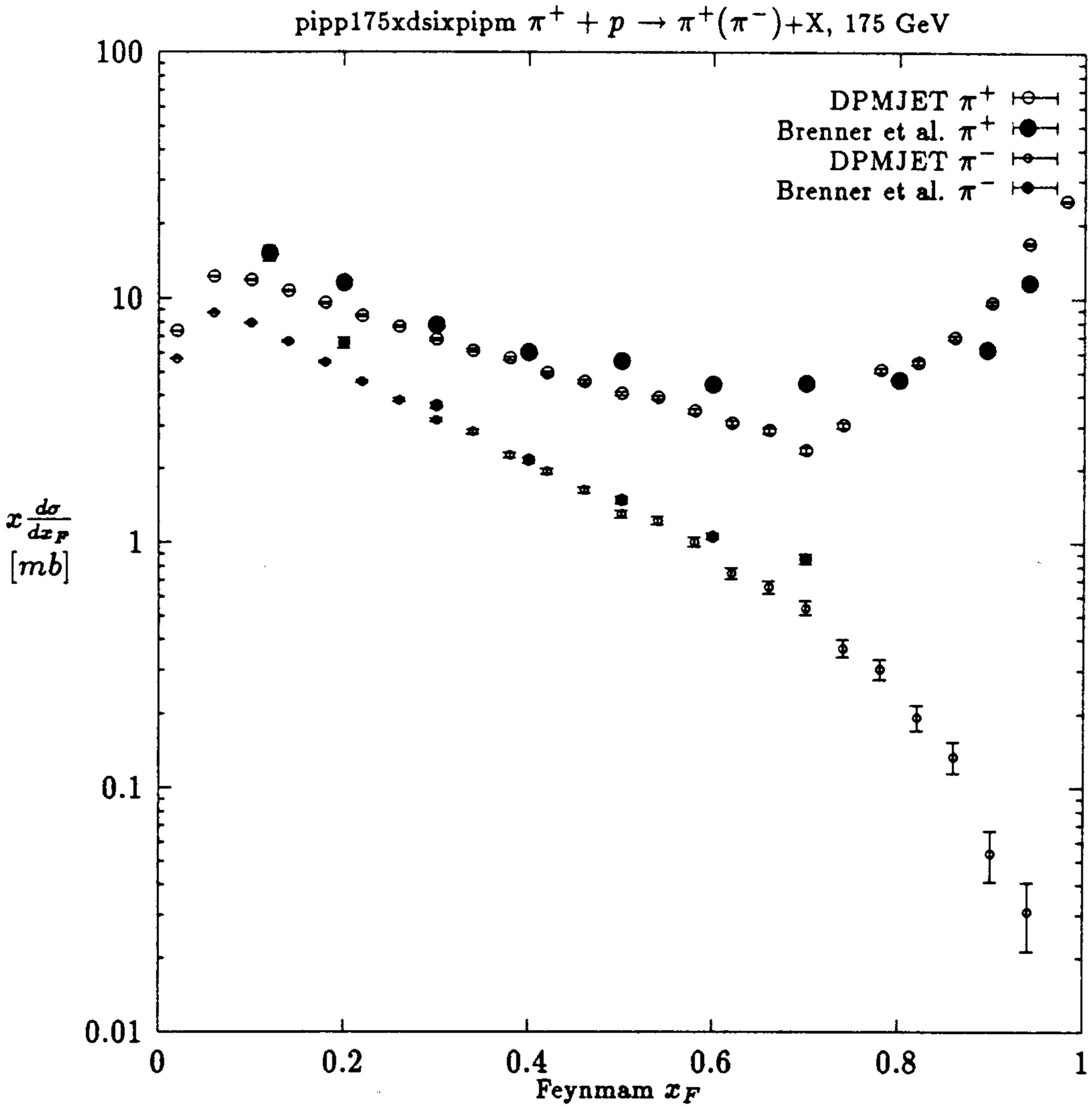
pipp175xdsixpipm $\pi^+ + p \rightarrow \pi^+(\pi^-)$+X, 175 GeV
DPMJET π^+
Brenner et al. π^+
DPMJET π^-
Brenner et al. π^-
$x\frac{d\sigma}{dx_F}$ $[mb]$
100
10
1
0.1
0.01
0
0.2
0.4
0.6
0.8
1
Feynmam x_F

Figure 20.

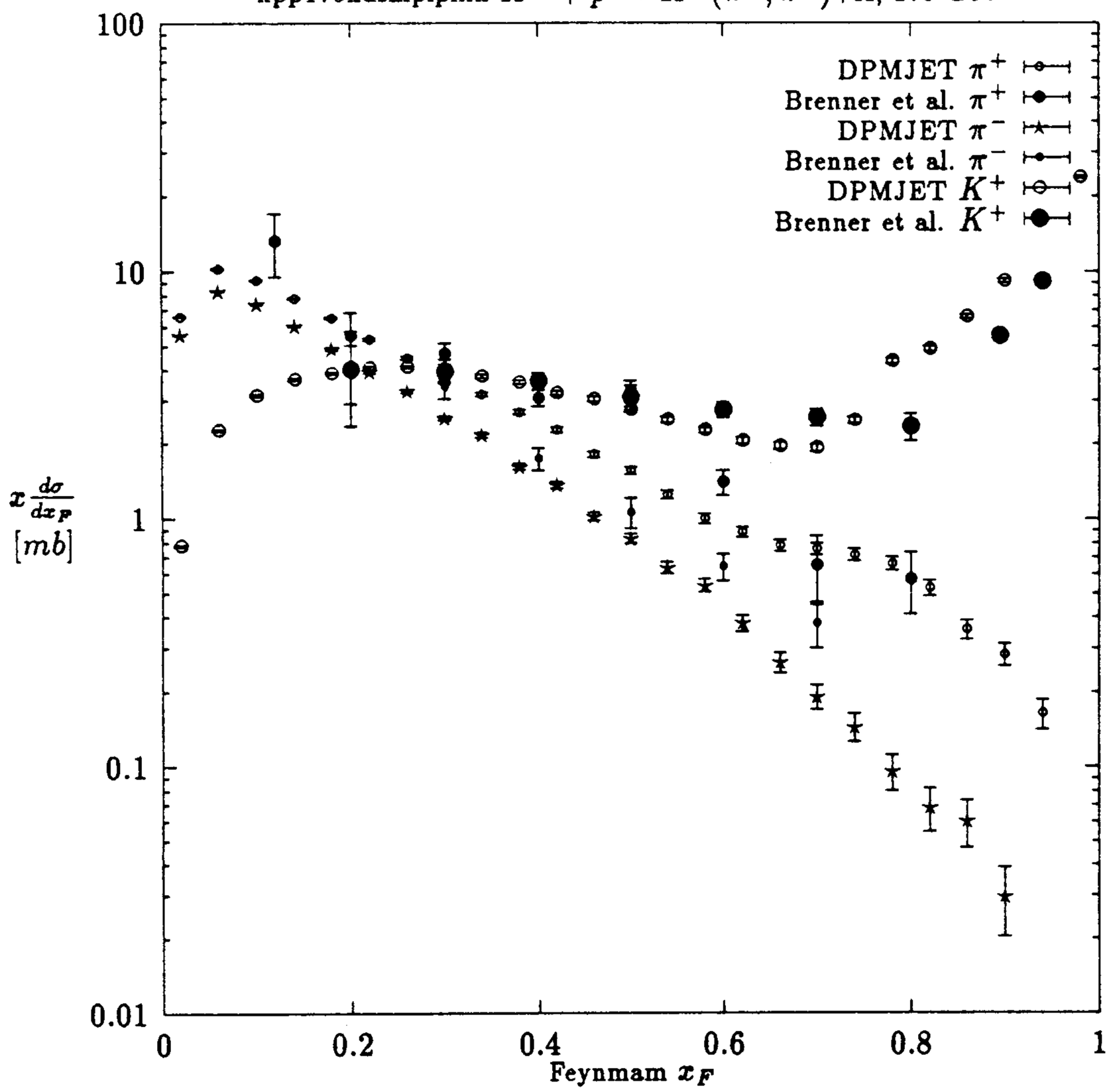
kpp175xdsixpipmk $K^+ + p \rightarrow K^+(\pi^+, \pi^-)$+X, 175 GeV
DPMJET π^+
Brenner et al. π^+
DPMJET π^-
Brenner et al. π^-
DPMJET K^+
Brenner et al. K^+
$x\frac{d\sigma}{dx_F}$ $[mb]$
100
10
1
0.1
0.01
0
0.2
0.4
0.6
0.8
1
Feynmam x_F

Figure 21.

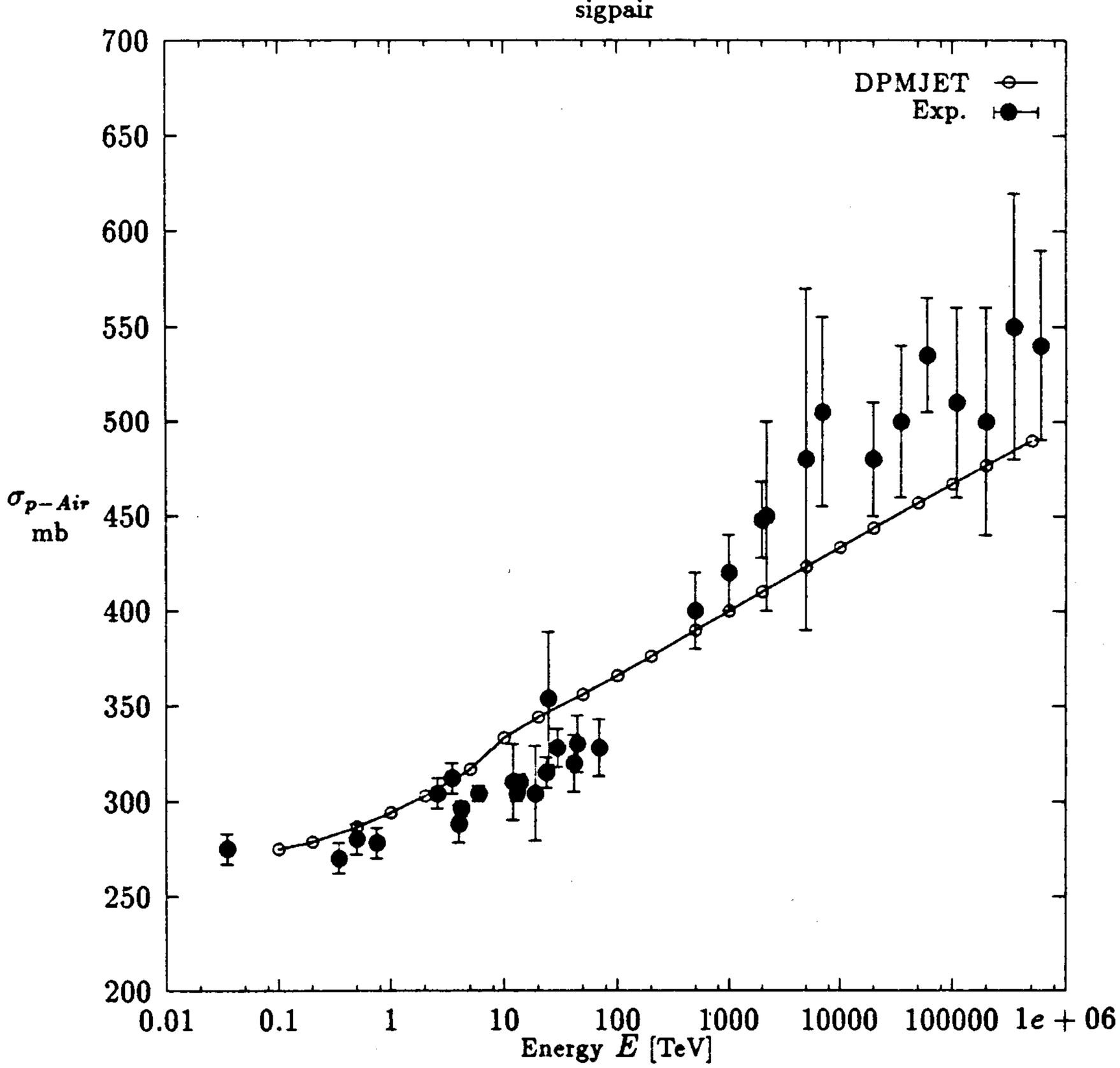
sigpair
DPMJET
Exp.
σ_{p-Air} mb
700
650
600
550
500
450
400
350
300
250
200
0.01
0.1
1
10
100
1000
10000
100000
1e + 06
Energy E [TeV]

Figure 22.

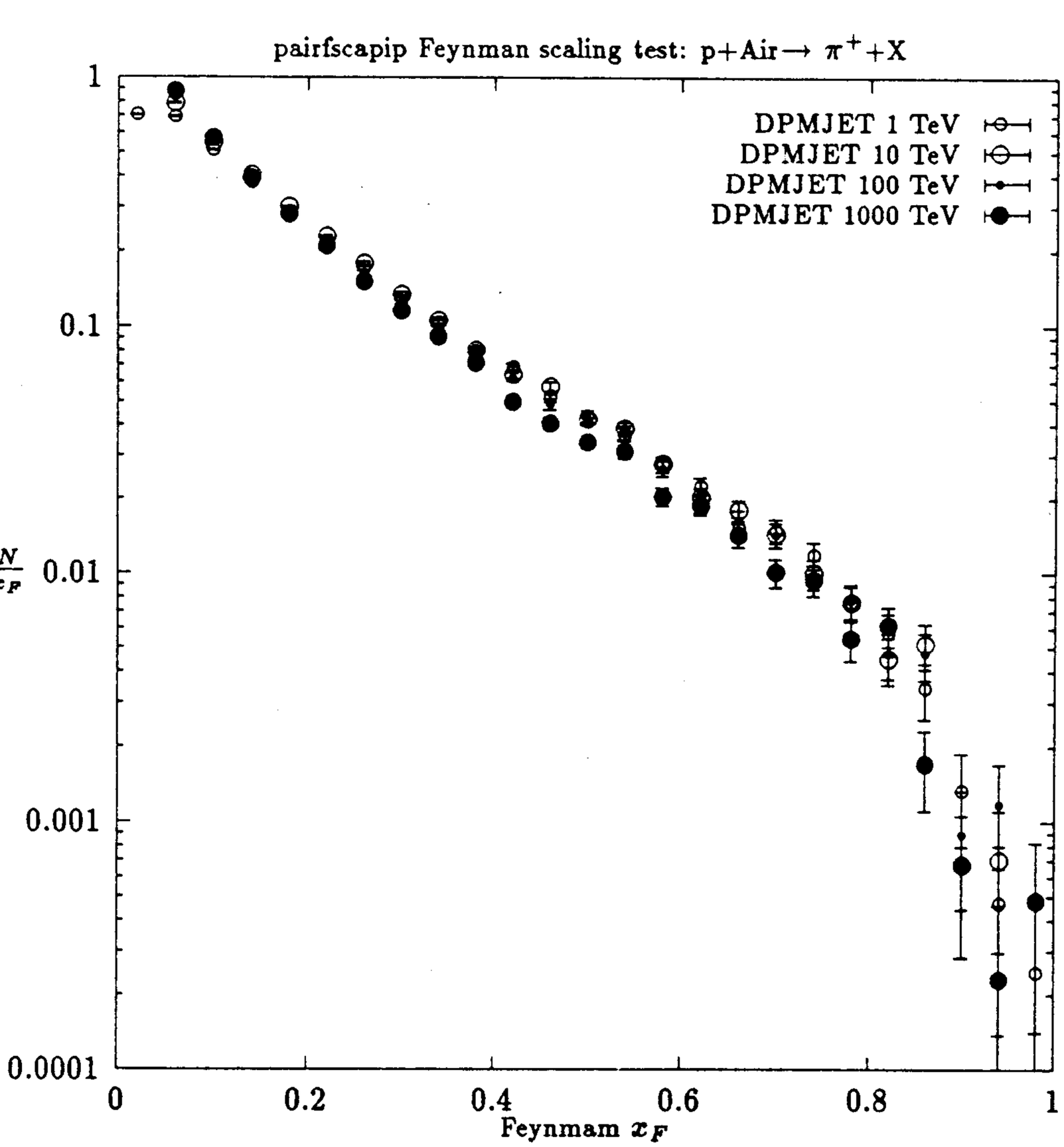
pairfscapip Feynman scaling test: p+Air→ π^++X
DPMJET 1 TeV
DPMJET 10 TeV
DPMJET 100 TeV
DPMJET 1000 TeV
$x\frac{dN}{dx_F}$
1
0.1
0.01
0.001
0.0001
0
0.2
0.4
0.6
0.8
1
Feynmam x_F

Figure 23.

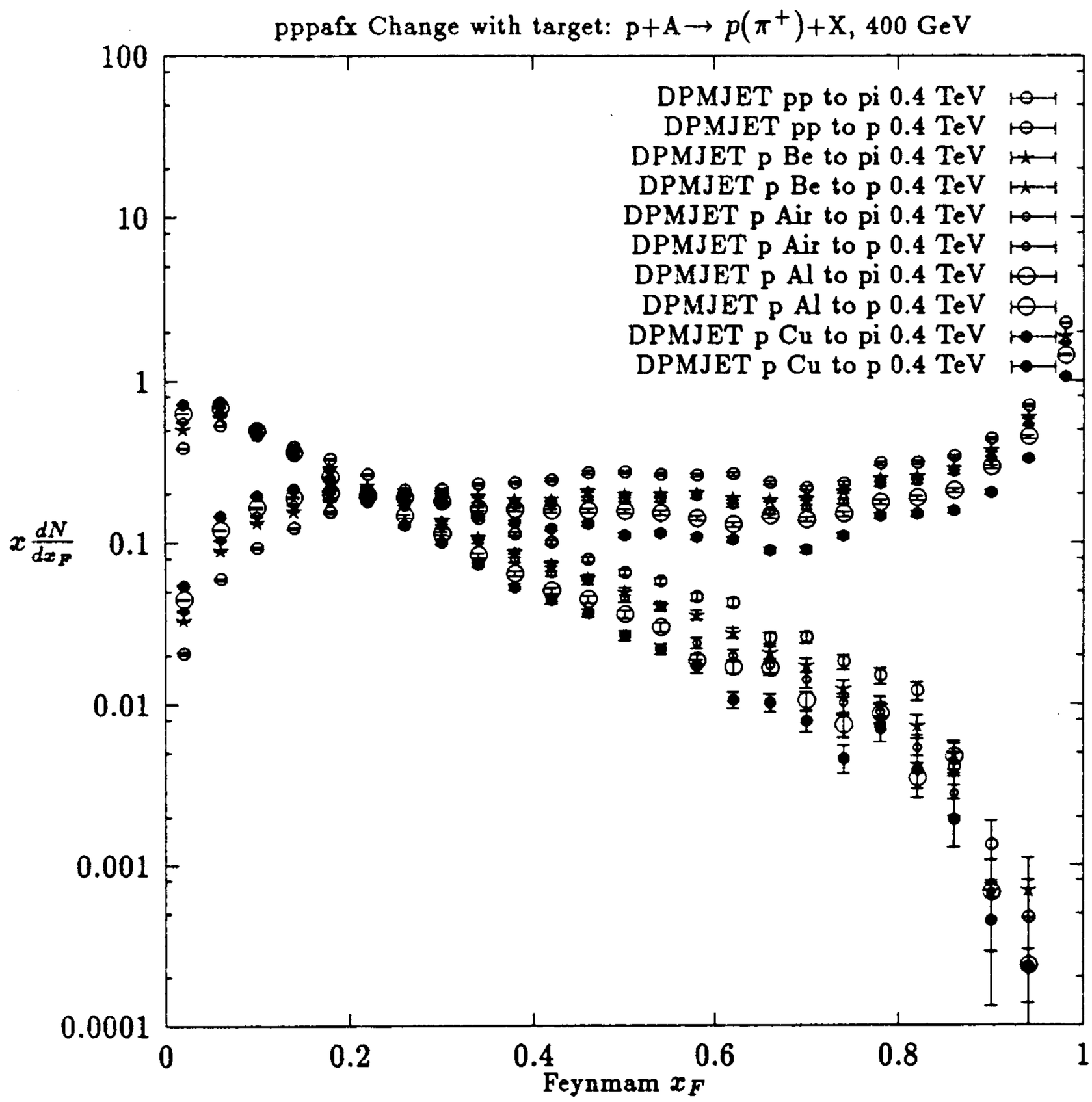
pppafx Change with target: p+A→ $p(\pi^+)$+X, 400 GeV
DPMJET pp to pi 0.4 TeV
DPMJET pp to p 0.4 TeV
DPMJET p Be to pi 0.4 TeV
DPMJET p Be to p 0.4 TeV
DPMJET p Air to pi 0.4 TeV
DPMJET p Air to p 0.4 TeV
DPMJET p Al to pi 0.4 TeV
DPMJET p Al to p 0.4 TeV
DPMJET p Cu to pi 0.4 TeV
DPMJET p Cu to p 0.4 TeV
$x\frac{dN}{dx_F}$
100
10
1
0.1
0.01
0.001
0.0001
0
0.2
0.4
0.6
0.8
1
Feynmam x_F

Figure 24.

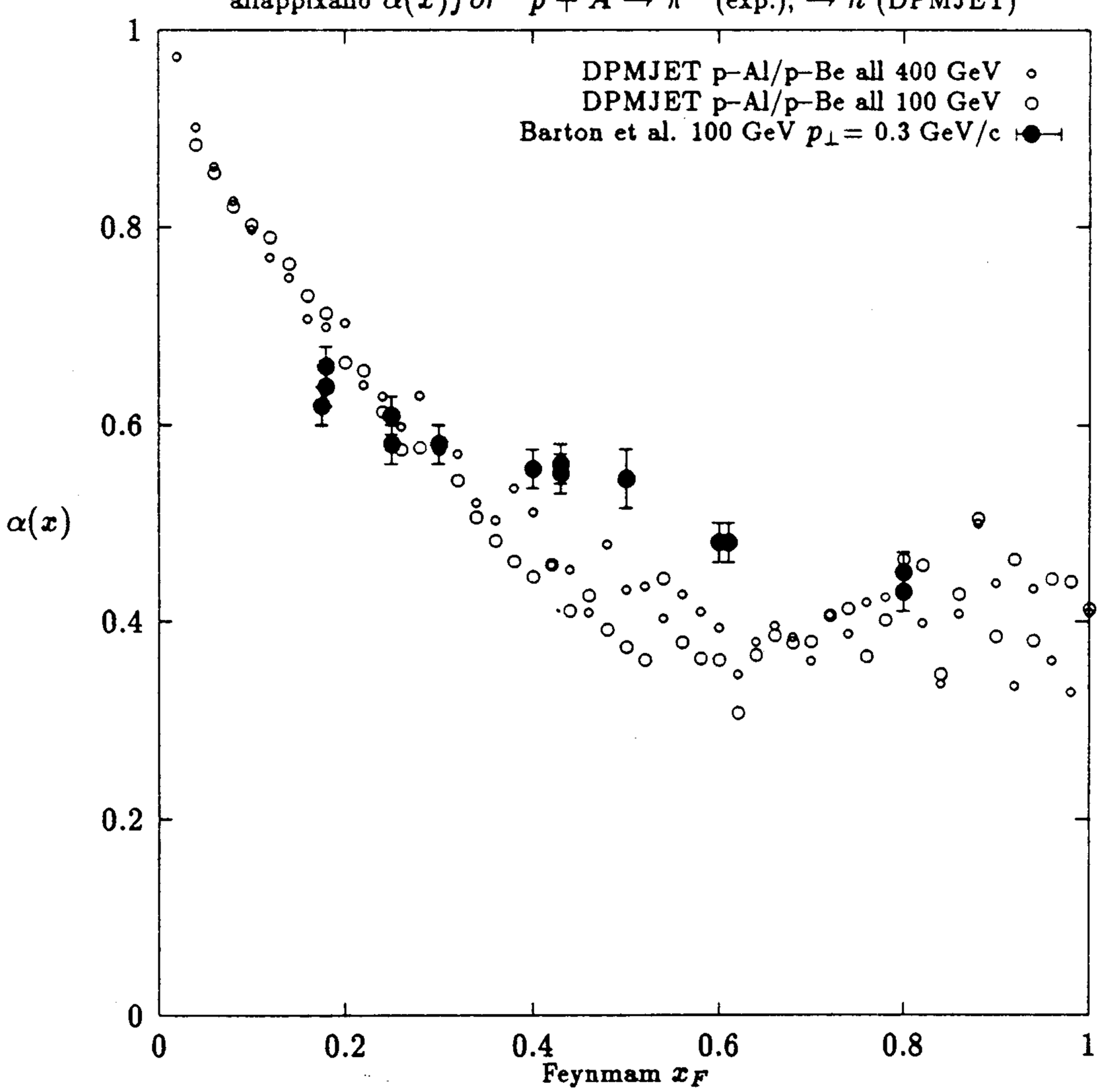
alfappixall6 $\alpha(x) for \quad p + A \rightarrow \pi^{\pm}$ (exp.); $\rightarrow h$ (DPMJET)
DPMJET p–Al/p–Be all 400 GeV
DPMJET p–Al/p–Be all 100 GeV
Barton et al. 100 GeV $p_\perp$ = 0.3 GeV/c
$\alpha(x)$
Feynmam x_F
0
0.2
0.4
0.6
0.8
1

Figure 25.

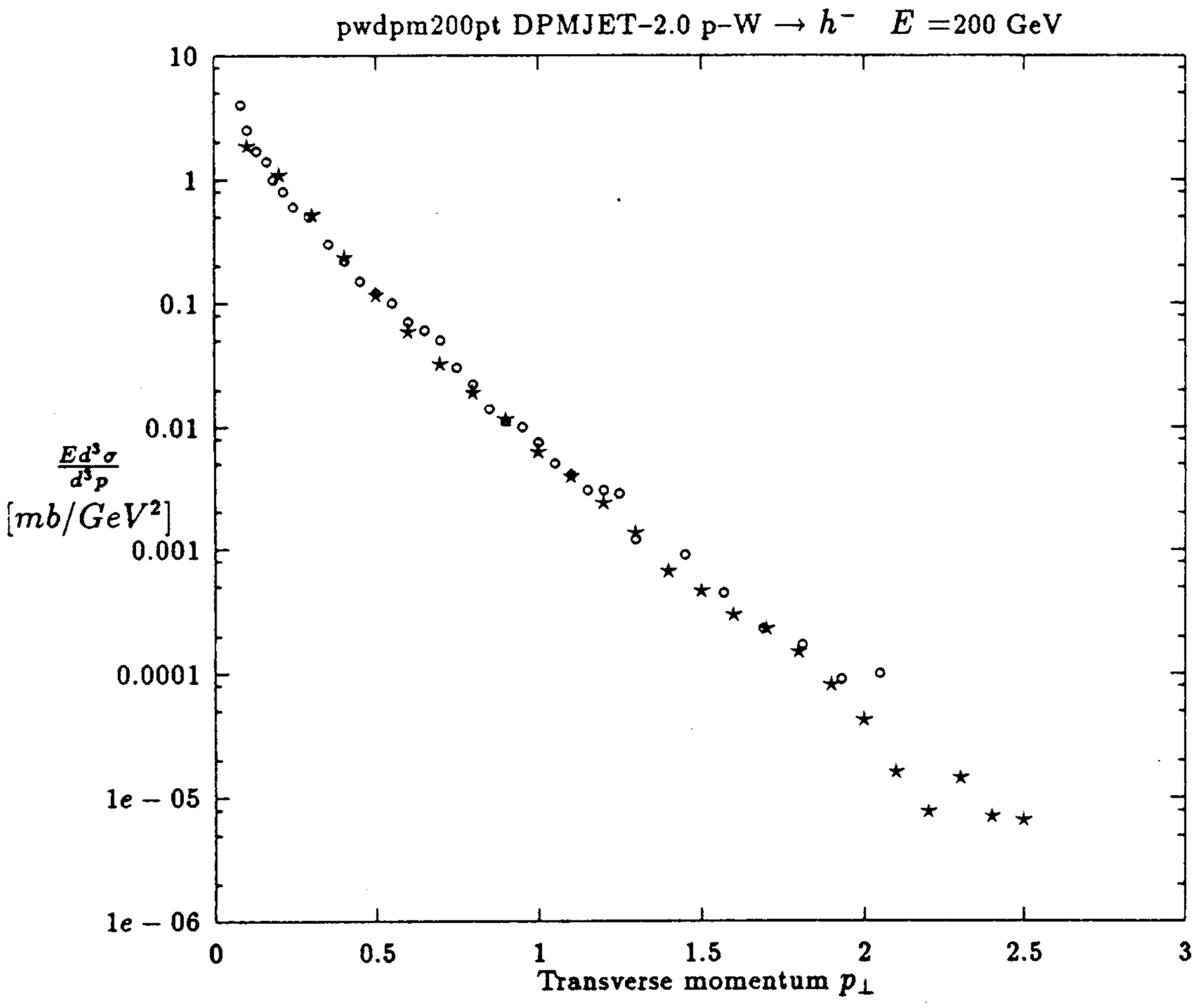
pwdpm200pt DPMJET-2.0 p–W $\rightarrow h^-$ E =200 GeV
$\frac{Ed^3\sigma}{d^3p}$
$[mb/GeV^2]$
10
1
0.1
0.01
0.001
0.0001
1e − 05
1e − 06
0
0.5
1
1.5
2
2.5
3
Transverse momentum $p_\perp$

Figure 26.

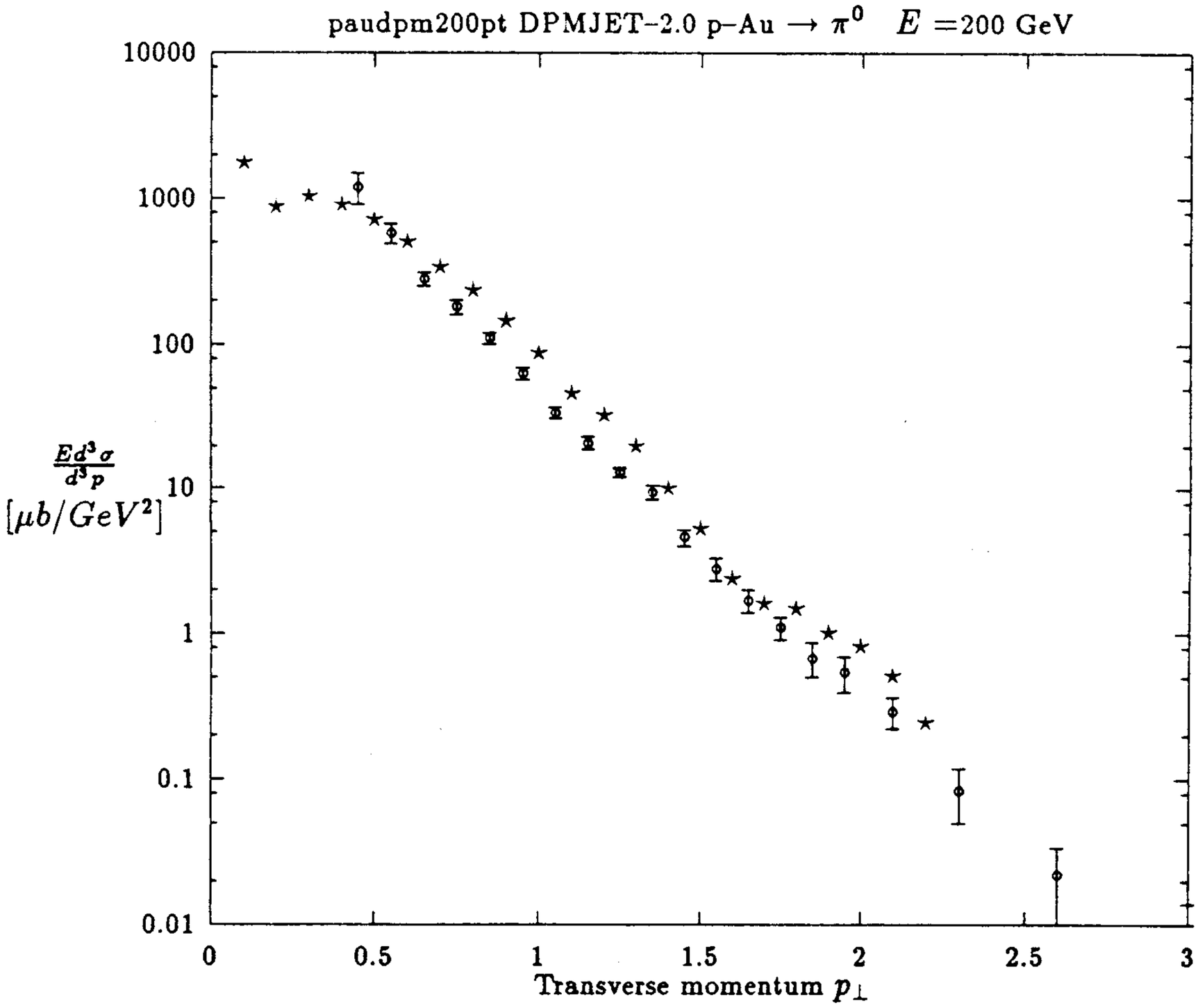
paudpm200pt DPMJET-2.0 p–Au → π^0 E =200 GeV
$\frac{Ed^3\sigma}{d^3p}$ $[\mu b/GeV^2]$
10000
1000
100
10
1
0.1
0.01
0
0.5
1
1.5
2
2.5
3
Transverse momentum $p_\perp$

Figure 27.

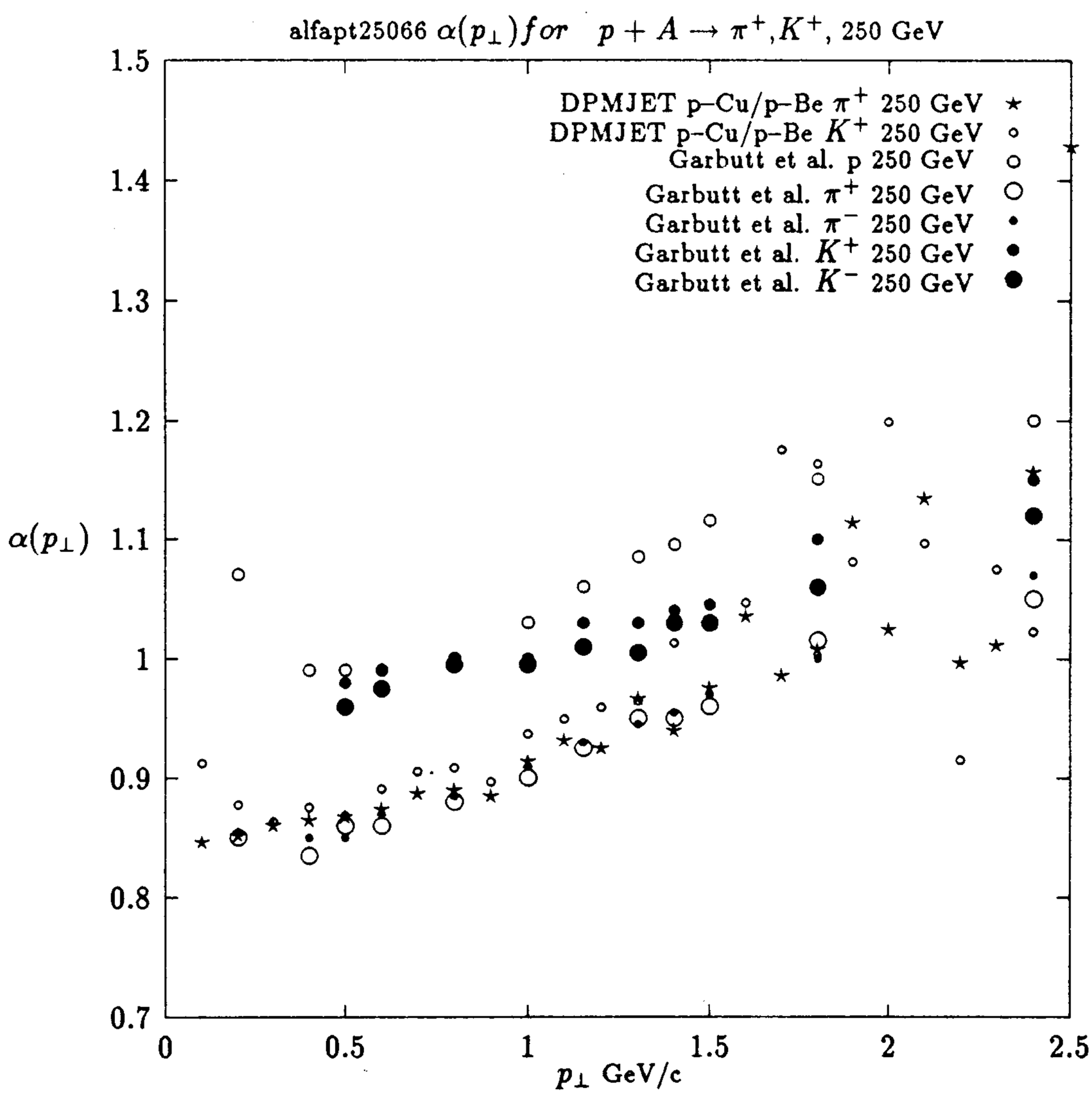
alfapt25066 $\alpha(p_\perp) for \quad p + A \rightarrow \pi^+, K^+$, 250 GeV
DPMJET p–Cu/p–Be π^+ 250 GeV
DPMJET p–Cu/p–Be K^+ 250 GeV
Garbutt et al. p 250 GeV
Garbutt et al. π^+ 250 GeV
Garbutt et al. π^- 250 GeV
Garbutt et al. K^+ 250 GeV
Garbutt et al. K^- 250 GeV
$\alpha(p_\perp)$
1.5
1.4
1.3
1.2
1.1
1
0.9
0.8
0.7
0
0.5
1
1.5
2
2.5
$p_\perp$ GeV/c

Figure 28.

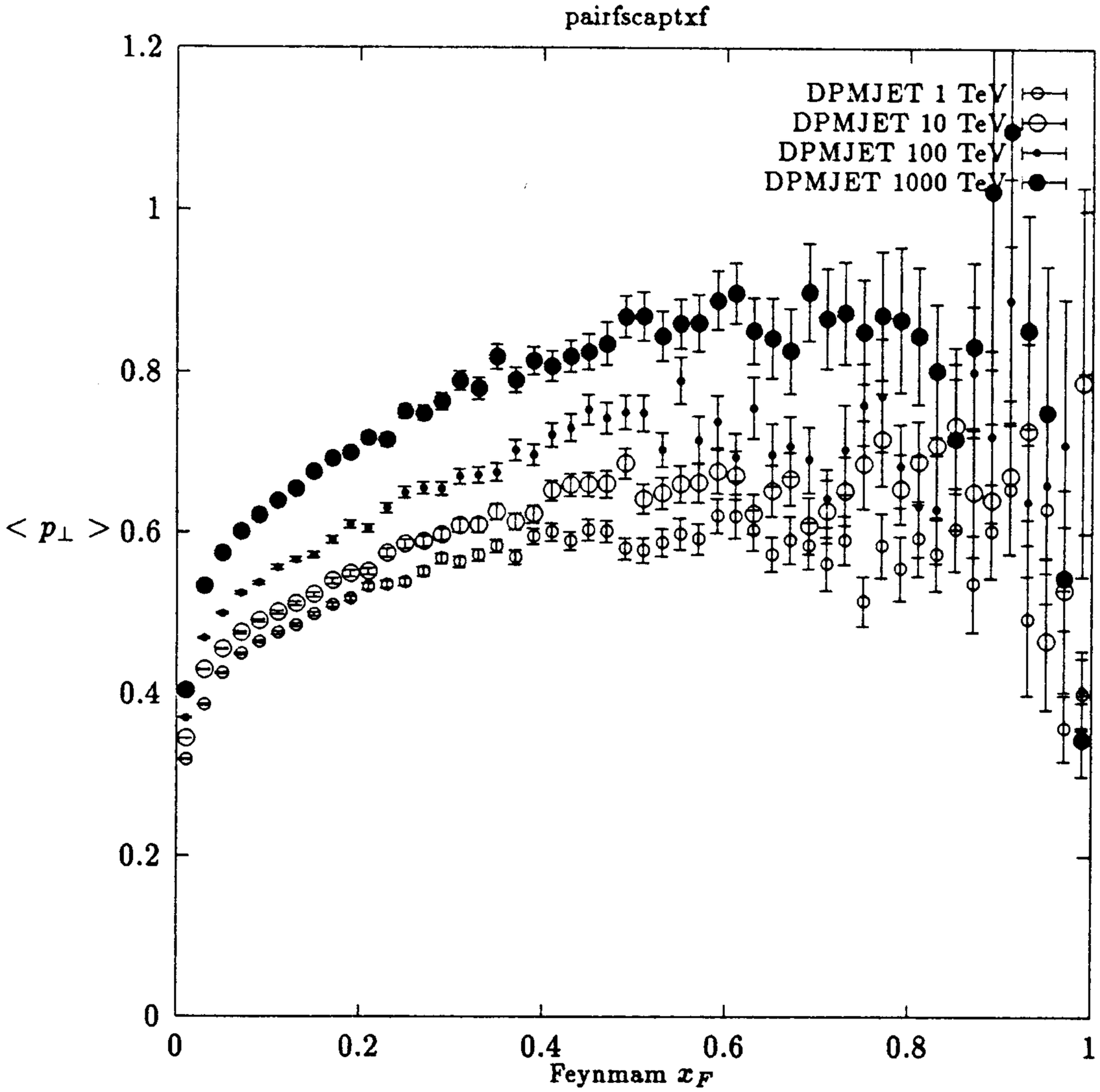
pairfscaptxf
DPMJET 1 TeV
DPMJET 10 TeV
DPMJET 100 TeV
DPMJET 1000 TeV
< $p_\perp$ >
Feynmam x_F
0
0.2
0.4
0.6
0.8
1
1.2

Figure 29.

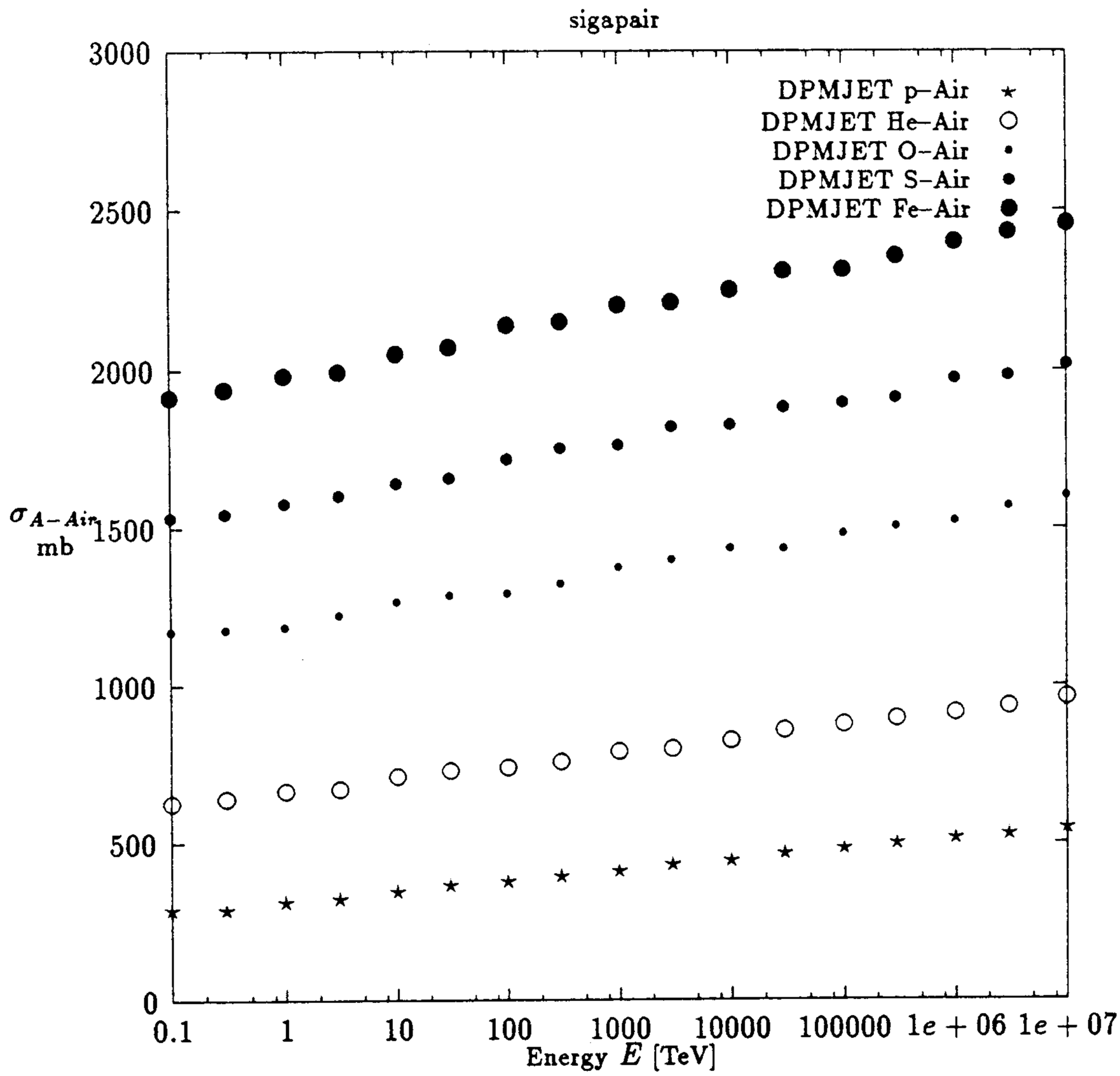
sigapair
DPMJET p–Air
DPMJET He–Air
DPMJET O–Air
DPMJET S–Air
DPMJET Fe–Air
σ_{A-Air} mb
3000
2500
2000
1500
1000
500
0
0.1
1
10
100
1000
10000
100000
1e + 06
1e + 07
Energy E [TeV]

Figure 30.